

DK 621.785.72:669.14-87.2

Ch 47

UDC 621.785.72:669.14+620.175:669.14-157.2

ACTA POLYTECHNICA SCANDINAVICA

CHEMISTRY INCLUDING METALLURGY SERIES No. 47

The Effect of Tempering on the Toughness of Hardened Steel

JUHA PIETIKÄINEN

Research Center of the Defence Forces

Thesis for the degree of Doctor of Technology accepted by the Institute of Technology, Helsinki.

HELSINKI 1966

P R E F A C E

The present work has mainly been carried out in the Physical Laboratory of the Research Centre of the Defence Forces, during 1965. The electron microscopy was done principally at the Institute of Electron Microscopy, University of Helsinki, but also at the Laboratories of Physics and Physical Metallurgy, Institute of Technology, Otaniemi.

Warm thanks are due to my teacher, Professor H. M. M i e k k - o j a, Ph. D., from whom I received very great help at the different phases of my work and particularly in its finishing stage.

I also wish to thank the Oy Wärtsilä Ab Helsinki Works and in particular Mr. K. T o i v o n e n, M.Sc. (Eng.), and Mr. K. K ä r k k ä i n e n, M.Sc. (Eng.), for the manufacturing of the torsion testing machine. I am also obliged to the staff of the Physical Laboratory of the Research Centre of the Defence Forces, especially Mr. T. H a r a v u o r i, for their help with the experiments.

Economical support has been received from Tekniikan Edistämissäätiö (Foundation for the Promotion of Technology) and from Suomen Luonnonvarain Tutkimussäätiö (Research Fund for the Natural Resources in Finland), which is gratefully acknowledged.

Finally I have the pleasure in thanking Mr. U. A t t i l a, M.Sc., who translated the manuscript into English.

Helsinki, December 1965,

The Author.

CONTENTS

| | |
|--|----|
| 1. Introduction | 7 |
| .1 The brittleness phenomena in hardened and tempered steel | 7 |
| .2 The causes of irreversible brittleness anomalies | 10 |
| .1 The brittleness of untempered martensite | 10 |
| .2 Brittleness phenomena associated with tempering | 10 |
| .3 Methods and equipment used in investigating the irreversible brittleness anomalies | 13 |
| .1 Micro-structure | 13 |
| .2 Mechanical tests | 13 |
| .4 Aims of the present work | 15 |
| 2. Experimental methods and procedures | 16 |
| .1 Material | 16 |
| .2 Heat treatment | 18 |
| .3 Micro-structure | 19 |
| .1 Dilatometry | 19 |
| .2 Carbide separation | 20 |
| .3 X-ray examinations | 20 |
| .4 Electron microscopy | 21 |
| .4 Mechanical tests | 22 |
| .1 Torsion test | 22 |
| .2 Calibrations and checks associated with the torsion tests | 28 |
| .3 Notched-bar impact test | 29 |
| 3. Results | 30 |
| .1 Undeformed structure | 30 |
| .1 Dilatometric observations | 30 |
| .2 X-ray examinations | 33 |
| .3 Electron microscopy | 36 |
| .2 Mechanical tests | 40 |
| .1 Torsion tests at various speeds | 40 |
| .2 Torsion tests at various temperatures | 49 |
| .3 Influence of tempering temperature on the results of the torsion test and notched-bar impact test | 55 |
| .3 Deformed structure | 58 |
| 4. Discussion | 65 |
| .1 Work hardening | 65 |
| .2 Effects of testing temperature | 67 |
| .1 Level of the $\tau/tg \gamma$ curves | 67 |
| .2 Shape of the $\tau/tg \gamma$ curves | 68 |
| .3 Effects of speed of rotation | 69 |
| .1 Heating of the test bar | 69 |
| .2 Concentration of deformation | 72 |
| .3 Pulsating deformation | 73 |
| .4 Other effects of speed of rotation | 74 |
| .4 Effect of tempering temperature on the toughness of hardened steel | 75 |
| Summary | 77 |
| References | 79 |

1. INTRODUCTION

One of the central aims in metal research is improvement of the strength of metals. In an attempt to achieve this in iron, the most important service metal, one approach is to take advantage of the high potential strength of martensite containing carbon. Unfortunately, this has been impeded by the extreme brittleness of carbon martensite. In order to improve the toughness, martensite is decomposed by tempering, but some potential strength of the martensite is lost in this operation. Raising the tempering temperature, that is, more thorough decomposition of the martensite, does not result in steadily increasing toughness; on the contrary, it may in fact lead to brittleness greater than that present in untempered martensite.

1.1 The brittleness phenomena in hardened and tempered steel

The toughness of steels of different composition varies in a highly complex manner, primarily according to the tempering temperature. The various testing methods reveal the variations in toughness differently. Fig. 1 shows the impact toughness curves, determined in two different ways at room temperature, and the yield strength curve of a Cr-Ni steel. Curve No. 1 represents the values of the torsion impact toughness and curve No. 2 those of the Izod impact toughness, both as functions of the tempering temperature. It can be seen that the torsion impact curve has a maximum at a temperature of about 200 °C and that a minimum occurs at about 300 °C, where the impact toughness drops even below the values found at about 100 °C. The curve derived from Izod tests shows a less pronounced maximum and minimum. The yield strength curve No. 3 descends uniformly in the direction from left to right along the tempering temperature axis.

The peak occurring in the impact test curves around 200 °C is also seen in the use of steels. Tools, for instance, which have been tempered to this range are superior in durability not only to untempered tools but also to those tempered in the minimum range.

Highly alloyed steels present other anomalies in the range of higher tempering temperatures and the shape of their torsion impact toughness vs. tempering

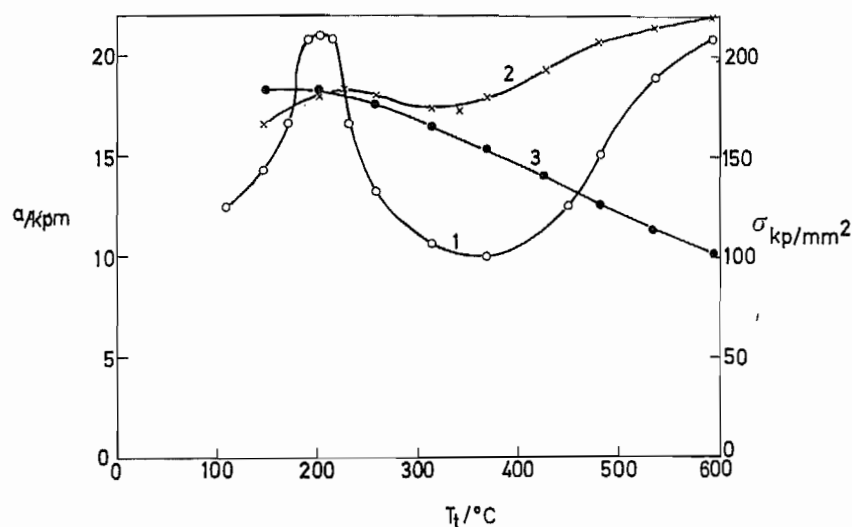


Fig. 1.

The effect of tempering on (1) torsion impact toughness, (2) Izod impact toughness and (3) yield strength of hardened Cr-Ni steel (0.50 % C, 1.30 % Cr, 0.20 % V.; austenitizing temperature $T_\gamma = 857^\circ\text{C}$, W. q). [1].

temperature curves may consequently be more complex than that shown in Fig. 1 [2].

Fig. 2 is a schematical presentation of the transition temperature of hardened steel in dependence on the tempering temperature, determined by the type of failure of notched-bar impact test specimens [3]. It can be seen that the transition temperature vs. tempering temperature curve has a maximum in the same temperature range in which the torsion impact curve has its minimum according to Fig. 1. A rise in this transition temperature is thus an indication of increased brittleness, too. Distinct correlation has been established in these tests between the type of failure and the rise in transition temperature. In specimens tempered in the 300 °C brittleness region, the fracture proceeds along the grain boundaries of the inherent austenite [3] as in untempered martensite [4], whereas its course deviates from these grain boundaries in specimens tempered at other temperatures.

No similar correlation exists for the failure of torsion impact test bars fractured at room temperature [5, 6].

In some alloyed steels, tempering around 500 °C has been found to produce a rise in the transition temperature as illustrated by Fig. 3 [7]. This manifestation of brittleness is called temper brittleness. In this instance, too, the phenomenon has been observed that fracture proceeds along the grain boundaries of the inherent austenite in the notched-bar impact test. The fundamental difference between temper brittleness and other brittleness phenomena resulting from tempering is the reversible character of temper brittleness. The brittleness disappears when the steel is heat-treated at a temperature

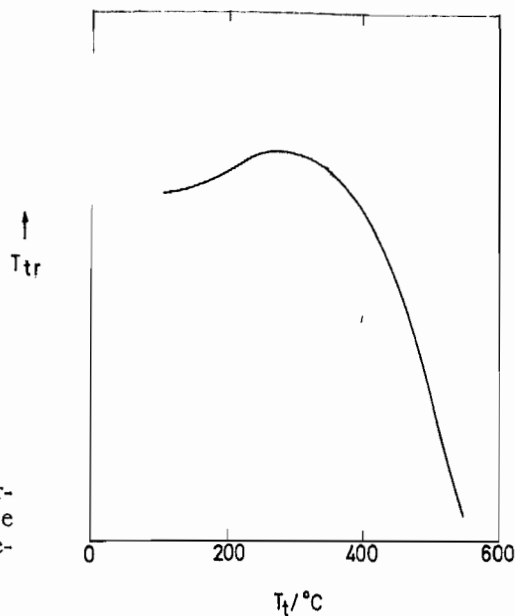


Fig. 2.

The effect of tempering on the transition temperature of hardened steel, determined by the type of failure of notched-bar impact test bars (schematic presentation). [3].

above the brittleness range and reappears on renewed tempering in the range producing temper brittleness [7]. Temper brittleness also occurs in structures other than those resulting from martensite decomposition.

The brittleness associated with the 300 °C tempering range differs from temper brittleness in that it is irreversible in character. Tempering at higher temperature completely cancels the brittleness in question so that it does not recur on subsequent tempering at 300 °C unless the specimen is once more austenitized and quenched [3]. The character of the other brittleness anomalies seen from the impact toughness curves has not yet been fully clarified and it is not known whether they are reversible or not.

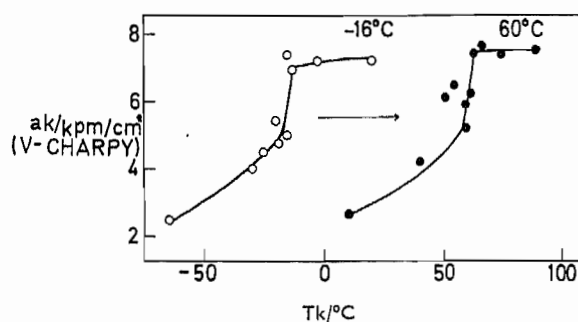


Fig. 3.

The effect of temper brittleness on the transition temperature of Cr steel (0.51 % C, 0.38 % Mn, 0.014 % P, 0.013 % S, 0.20 % Si, 0.06 % Ni, 2.96 % Cr). Tempered martensitic structure, heat treatment: $\frac{1}{2}$ hr at 900 °C, quenching in oil, and subsequently: (1) tempering 1 hr at 650 °C, quenching in water (white circles), (2) tempering 24 hrs at 525 °C, quenching in water (black circles). [7].

1.2 The causes of irreversible brittleness anomalies

1.2.1 The brittleness of untempered martensite

The brittleness of untempered martensite is commonly considered to be a property of the martensitic state in itself. Little research has been done concerning the causes responsible for this brittleness. Some conjectures have been presented: for instance, it has been attributed to the macro- and micro-stresses produced at transformation [5]. However, recent investigations made by the author indicate that the brittleness may, partially at least, result from the changes occurring in the martensite during the quenching process and subsequently at room temperature [6].

1.2.2 Brittleness phenomena associated with tempering

Past literature tends to the basic assumption that the toughness of martensite increases steadily with increasing tempering temperature, while its decomposition gradually progresses at the same time. The toughness minima observed in connection with tempering would be anomalies.

The 300 °C brittleness region

The hypothesis of decomposition of the retained austenite. The brittleness occurring in the tempering temperature range around 300 °C has been recognized for some time. The first explanation for this brittleness phenomenon was probably given in 1924 by Grossman [8], who thought that it was caused by the decomposition of retained austenite in

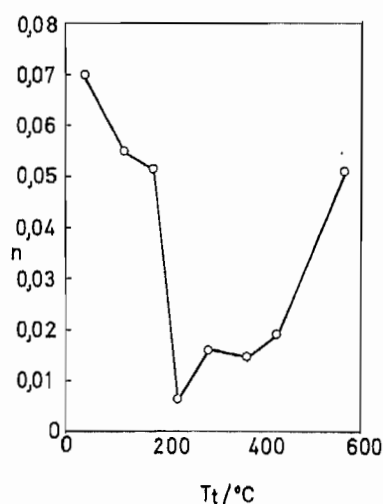
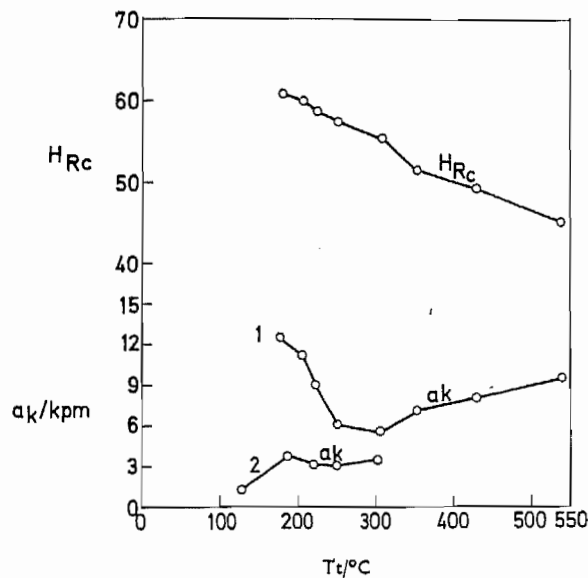


Fig. 4.
The effect of tempering on the values of the work-hardening exponent of hardened carbon steel (0.75% C, 0.9 % Mn, 0.9 % Mo). [11].

Fig. 5.
The effect of tempering on (1) torsion impact toughness and (2) notched-bar impact toughness of hardened carbon steel (0.72 % C). [11].



one way or another. The phenomenon had been studied even before him, but no elucidation of its causes had been attempted.

The same explanation was put forward in 1934–1935 by Luerssen and Greene in their thorough investigations [5, 9], which dealt with the effect exerted on the toughness of steel by impurities, austenitizing temperature and tempering time.

The hypothesis based on brittleness of cementite. In their above-mentioned investigations, Luerssen and Greene suggested as another possible cause of brittleness, the growth of ferrite grains up to a certain, unspecified critical order of size and increasing coarseness of the cementite.

In recent research, similar results have been reached e.g. by Lement et al. [10], who attributed the brittleness phenomenon to cementite precipitated at grain boundaries.

The hypothesis of mechanical instability. In 1948, Read et. al. [11] studied the plastic deformation and fracture of hardened steel. They determined the stress-strain curve in slow compression tests, and the toughness by means of torsion impact tests and notched-bar impact tests. Test specimens of identical heat treatment were prepared for each testing procedure.

In Fig. 4, the values of the exponents of work hardening n in Mayers form $\sigma = a\varepsilon^n$, calculated from the compression diagrams, have been plotted over the tempering temperature range. In Fig. 5, the values of torsion impact toughness and Izod toughness have been presented as functions of

the tempering temperature. The curve representing the work hardening exponent and the impact toughness curves have their minimum in the same tempering temperature range. Read et al. [11] presumed that these anomalies must be interconnected and that the minimum in the torsion impact curve is attributable to the small amount of work hardening on cold-working and to heating of the specimen. It is to be noted that the test bar is heated in the torsion impact test by reason of the working that takes place. Such a temperature rise results in reduced resistance against deformation in numerous materials. According to Read et al., this would lead to mechanical instability of the torsion impact test and, finally, to fracture by shearing. It is obvious that this will occur most easily in the region of low rate of work hardening. — A different explanation was suggested by Read et al. for the anomaly observed in the notched-bar impact curve: they thought that the extent of the deformed area produced at the fractured surface is dependent on the work hardening; this area would be narrow when the work hardening is low.

In 1957, Polakowski [12] also investigated the possibility of mechanical instability. However, he ascribed the effect of the brittleness-causing factors, high loading rate, notched specimens and low temperatures, to their tendency to raise primarily the yield point while the fracture stress would not be affected.

The hypothesis of impurities. Schrader et al. [13], in 1950, and Payson [14], in 1951, succeeded in eliminating the brittleness by alloying the steel with aluminium and titanium. Both maintained that the brittleness resulting from tempering around 300 °C is caused by the segregation of nitrides. When the nitrogen is bound in insoluble compounds, no brittleness would occur.

In 1960, Capus et al. [15] investigated iron-carbon alloys of high purity and demonstrated that no brittleness occurs in the region of 300 °C. In otherwise pure steel to which antimony, phosphorus, tin, arsenic or nitrogen had been added, however, the brittleness region was again observed. In notched-bar impact tests at room temperature, only the steel containing nitrogen suffered fracture along the grain boundaries of the inherent austenite in a manner identical with that of commercial steel with the same carbon content, which was also included in the tests.

In 1963, Capus [3] attempted to relate the impurity hypothesis and the hypothesis concerning the brittleness of cementite. He thought that brittleness is not only caused by the segregation of cementite alone but also by simultaneous influence of impurities, although no differences in structure can be seen between pure steel and the corresponding commercial steel.

1.3 Methods and equipment used in investigating the irreversible brittleness anomalies

1.3.1 *Micro-structure*

Methods to elucidate changes in micro-structure occurring during the tempering of steel include changes in magnetic properties [9, 16], electrical conductivity [17] and specific volume [9, 18]. X-ray methods have been used for observations concerning the matrix [19, 20] and the segregation of carbides [18, 19]. Frequent use has been made of optical and electron microscopy. The last-mentioned approach, in particular, has done much to further the understanding of the phenomena involved, although certain technical difficulties had to be overcome [20, 21]. The complete list of relevant references would be extensive, and only a few have been mentioned here.

On the other hand there are very few publications concerning optical and electron microscope studies of the deformed micro-structure [20, 22].

1.3.2 *Mechanical tests*

Notched-bar impact and torsion impact tests have been most used. Le Chatelier [23] probably invented the notched-bar impact test, the idea of which was first presented by him in 1892 to the French Committee on Methods of Testing. The Charpy and Izod tests, which are used nowadays, have been developed from it [24]. The tests are conducted either with an unnotched or a notched test bar, and the energy consumed in rupturing the bar is found from the height to which the impact pendulum swings. This, in fact, accounts for all the information obtainable from a bending test of this kind. The stress-strain relationship in the test bar at the moment of rupture is complex, particularly so in a notched test bar. In order that tests might be conducted under less complicated stress-strain conditions, facilities for tensile impact tests have been provided in modern, commercial impact testing machines. In this test, the test bar is ruptured by tension; the energy consumed in the process is again measured by the maximum height which the pendulum attains.

In 1933, Luerssen and Greene [25] designed the torsion impact testing machine schematically presented in Fig. 6. The solid, round test bar (P) is ruptured by sudden torque provided by the heavy flywheel (S), which supplies the requisite breaking energy. The test is initiated by coupling the test bar with the aid of a slip-free clutch (Q, N) to the flywheel, which has been brought up to a given speed of rotation. This is accomplished by pushing the keyed slide (H) towards the flywheel so that the clutch bar (Q) engages

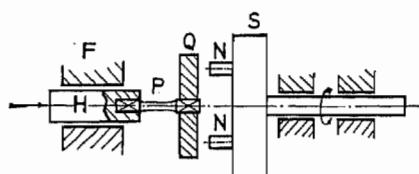


Fig. 6.
Schematic drawing of the torsion impact testing machine. [25].

with the dogs (N). The key and keyway prevent the slide (H) from turning with reference to the machine bed (F) and the flywheel will therefore twist the test bar in two, suffering a loss of speed in the process. The energy consumed in rupturing the specimen is obtained from the difference in speed, taking into account the energy stored in the clutch element (Q).

In the course of a test of this kind the speed of rotation slows down. Moreover, when a solid test bar is used, the shearing strain and its rate of change decrease from the surface of the bar towards its interior. Correction formulae derived by various approaches have been presented in attempts to eliminate the first-mentioned drawback [26]. It should also be noted that the twist is not always uniformly distributed over the narrow neck portion of the test bar [27], and it is therefore impossible to obtain stress-strain diagrams by means of tests conducted in this manner.

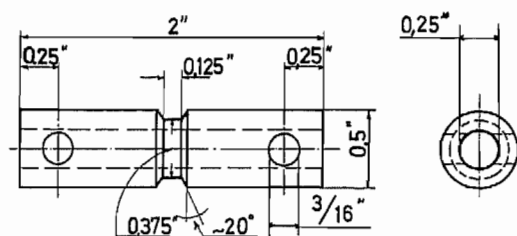


Fig. 7.
Hodierne's tubular test bar. [28].

In order to avoid these difficulties, H o d i e r n e [28] introduced a hollow, tubular test bar, Fig. 7. His aim was to create simple test conditions, in which graphs of true stress vs. true strain might be obtained. By reason of the small wall thickness, the amount of shearing strain and its rate of change can be considered constant at each cross-section of the test bar. Hodierne made the neck portion of the test bar short and the transition zone strongly tapering, with sharply defined boundaries. This was meant to prevent buckling of the test bar and to ensure uniform distribution of the deformation over the neck portion in axial direction. However, the notch effect at the abrupt transitions between neck portion and clamping ends produces stress states, which cannot be measured, and the test bar suffers rupture at the point of transition. This occurred in experiments carried out by the author even when the test bars consisted of soft iron.

R e a d et al. [11] employed a compression test in order to be able to measure the stress-strain state. They used special attachments to compress test specimens having the form of a circular, straight cylinder in a standard testing machine and made simultaneous observations of the force and of the thickening of the cylinder. Lead sheets were inserted between the specimen end faces and the anvil faces of the compression attachment to provide lubrication and thus to reduce the friction. An advantage of this method is its applicability also in the testing of brittle substances. It has, however, the following drawbacks: presence of friction at the end faces; changes in the stress state by reason of the resultant barrelling of the specimen; the fact that the test cannot be continued up to rupture and toughness is therefore not measurable with its aid; and technical difficulties in arranging for high rates of loading.

1.4 Aims of the present work

The technological significance of the toughness of tempered steel is generally acknowledged and it has been much investigated on this account. Nevertheless, the results have been rather unrewarding, owing to practical as well as theoretical difficulties.

In principal, the reason for this has been the fact that it has not been possible, with the aid of existing testing methods, to follow satisfactorily the stress state and its development in tests conducted up to failure of the specimen.

The author therefore decided to include among the aims of the present work the design of a machine with which martensite could be deformed under controlled conditions. This must occur in a manner which enables the true stress-strain state to be recorded with reasonable accuracy throughout the course of deformation and up to the moment of rupture.

Thus, the purpose was not only to make accurate mechanical tests but also to carry out observations of the structures produced on tempering, in order that the tempered martensite might be compared to that encountered in other cases where the relationship between structure and stress-strain diagram is better understood. Further, an attempt was to be made to elucidate the causes responsible for variations in toughness.

2. EXPERIMENTAL METHODS AND PROCEDURES

A steel was especially alloyed for the present work, of the following nominal analysis: 0.35 % C, 20 % Ni, and 1.5 % Si. The test specimens made of this steel were austenitized, quenched in liquid nitrogen and isothermally tempered at various temperatures in the range $T_t = -110...450^\circ\text{C}$.

After this heat treatment, the specimens' structures were examined by x-ray and by electron microscopy, applying both the replica and the thin foil techniques. The changes in structure occurring during the tempering process were further followed by the aid of a dilatometer.

However, the principal part of the work consists of the mechanical testing experiments, for which a special torsion testing machine was designed.

2.1 Material

The following points were considered in choosing the constituents of the steel used in this work:

- The M_s temperature should be low in order that no tempering reaction might occur during quenching. For this to be positively guaranteed, the M_s temperature should be lower than -60°C [17].
- Since it is difficult to eliminate the effects of retained austenite, its amount should be made as small as possible and it should not decompose in the tempering process.
- In order to facilitate the heat treatment arrangements, the steel should have such an S curve that in its austenitic state it will not undergo decomposition even at fairly slow cooling rates and the A_{r1} temperature should also be high.
- However, the carbides formed on tempering should grow each in their own temperature interval so that it might be possible to investigate their effects separately. No special carbides should be formed, which would only add to the complexity of the problem in hand.
- The type of fracture should be the same for any given tempering temperature, because different types of fracture would be an impediment to comparison.

This list of desirable properties obviously contains certain requirements which tend to conflict with each other; accordingly, suitable compromises were sought in the selection of steel, and these are summarized as follows.

The aspired M_s temperature was fixed at $\pm 0^\circ\text{C}$ in order that the amount of retained austenite is less than 10 % and that the A_{r1} temperature would remain sufficiently high for the purpose in question.

In order to avoid special carbides and still achieve the specified aims, the steel was alloyed with Ni and Si. The addition of nickel was intended to lower the M_s temperature, while silicon had the task of separating the formation of ϵ carbide from that of Fe_3C [18].

According to earlier observations [6] concerning steel with a carbon content of $\text{C} \approx 0.35\%$, the torsion impact tests after tempering at any temperature resulted in fracture by shearing. The requirement was therefore chosen as starting point that the carbon content of the steel should be about 0.35 %. This is high enough to produce a distinct ageing effect in the martensite [17]. On the basis of data found in the literature [17, 18, 29, 30], the following analysis was ultimately chosen: $\text{C} = 0.35\%$, $\text{Ni} = 20\%$, and $\text{Si} = 1.5\%$. The hope was entertained that a steel of this composition would very nearly comply with all the specified requirements. It has to be understood that the properties of the steel could not be predicted with any great accuracy in advance, since information on the effects of the alloying elements was not available.

The steel was manufactured at the Imatra steel works of Vuoksenniska Oy by an industrial arc-melting procedure. The alloying elements were added in the ladle. In order to reduce the tendency of segregation, the steel was cast to form a horizontal, elongated ingot. The results of the quantitative analysis made at the steel works of the ingot are given in Table 1.

TABLE 1. Analysis of the steel investigated.

| C % | Ni % | Si % | Mn % | P % | S % | Cr % | Mo % | Cu % | Sn % | B % |
|------|-------|------|------|-------|-------|------|------|------|------|--------|
| 0.34 | 20.10 | 1.41 | 0.42 | 0.012 | 0.018 | 0.07 | 0.06 | 0.18 | 0.02 | 0.0004 |

Owing to the raw materials and the melting procedure, the steel contained a fair amount of impurities.

A billet was forged from the ingot and hot-rolled into a bar 13 mm in thickness, which was allowed to cool in air. Preliminary dilatometric examination revealed that the A_{r1} temperature was slightly above 500°C . Accurate determination of this temperature was difficult, because no distinct

transformation point could be noted. The M_s temperature was found to be about $+10^\circ\text{C}$ when the austenitizing temperature and time were $T_\gamma = 1000^\circ\text{C}$, $t_\gamma = 30$ min. When, following austenitizing, the steel was austempered at temperatures between 180 and 250°C for 25 minutes, signs of austenite decomposition were observed.

The structure of the steel after hot-rolling was metastable austenite. This caused extensive work hardening, which precluded machining of the steel. The entire quantity of steel needed for the investigation was therefore quenched in liquid nitrogen so that it acquired predominantly martensitic structure. The bars were then packed in a metal container and kept at 500°C for 24 hours. The hardness of the steel was about $300 H_V$ after this treatment. It could then be machined, although only with difficulty. The described annealing procedure proved to be the only possible method; annealing temperatures considerably in excess of 500°C caused austenization of the structure, while isothermal annealing at any temperature below 500°C in order to decompose the austenite resulted in even greater hardness than that attendant on the described hardening and annealing procedure.

2.2 Heat treatment

In order to overcome possible effects caused by the atmosphere, the test specimens were enclosed in quartz capsules evacuated to about 10^{-2} mm Hg pressure during the heat treatment.

The specimens were austenitized in a tube furnace. The temperature was measured with a Pt vs. Pt-Rh thermocouple. Temperature control and measurement were accomplished with an estimated accuracy of $\pm 5^\circ\text{C}$.

The austenitized specimens were quenched while still in the capsule to water of about $+20^\circ\text{C}$. When it was desired to investigate virgin martensite, however, quenching water of $+40^\circ\text{C}$ was used and the capsule was broken under water after the boiling had subsided. The specimen was transferred directly from the water into a heating chamber maintained at the same temperature, $+40^\circ\text{C}$, where the identifying inscriptions and markings needed in subsequent tests were made. This procedure of maintaining the specimen in austenitic state during the time required to perform the inscribing and then of quenching it (free of capsule) to liquid nitrogen so that the highest possible cooling rate from $+10^\circ\text{C}$ down to -60°C was achieved, served the purpose of minimizing the ageing of the martensite during quenching. The specimens intended to be tempered at room temperature or higher were quenched to liquid nitrogen in their capsules; since the capsules were not broken until after the tempering they were thus useful in protecting the specimen in the tempering treatment, too. It is felt that the quenching rate

at which the critical interval of $+10$ to -60 °C was traversed was not ideal and that some ageing of the martensite may have taken place on quenching. However, this effect was thought to be negligible in such cases.

The tempering treatments were made in baths with given temperatures to within ± 1 °C; these temperatures were measured by calibrated thermocouples for 200 °C or above, and with mercury-in-glass thermometers at lower temperatures. The accuracy of measurement was estimated to be ± 2 °C above 200 °C and better than ± 0.5 °C below this temperature.

The primary aim of the work was to investigate the structures produced on tempering and mechanical properties, employing an identical austenitizing treatment in all tests; variations in the austenitizing process affect the grain size of the inherent austenite and the martensite lens size, but it was not intended to include the effect of these factors among the objects of study. The coarse micro-structure resulting from a high austenitizing temperature facilitates the micro-structure observations. Accordingly, an austenitizing temperature of $T_{\gamma} = 1\,200$ °C was chosen and the austenitizing time was made $t_{\gamma} = 30$ min. The inherent austenite assumed a grain size of 3 (ASTM) as a result of this treatment. Measurement of the lens size proved to be difficult. The largest lenses were found to be about 0.06 mm in length.

In order to reduce the number of necessary experiments, endeavours were made to devise a simple tempering procedure. A choice could be made between tempering for different periods at one and the same temperature or at different temperatures for a fixed length of time. In the first instance a high temperature would have to be chosen so that the tempering processes might be completed within reasonable time. However, in this case the initial part of the tempering would take place so rapidly that the specimen would not have time to reach the tempering temperature desired before its occurrence, and it would thus be impossible to investigate the early part of the tempering process.

Experimental arrangements according to the second alternative yield a vertical section through the tempering temperature–tempering time system. All phases of tempering can be undertaken by gradually increasing the temperature if this approach is chosen. This method was accordingly adopted in the present work.

2.3 Micro-structure

2.3.1 Dilatometry

A dilatometer was built for investigation of the changes in micro-structure occurring during the tempering process. Its operating principle has been presented in Fig. 8. Concentrically placed quartz tubes B transmit the changes

in length of the test bar C to the inductive pick-up A. The signal thus produced by the pick-up is transmitted to a recorder by a carrier-wave amplifier. A test bar of small cross-section is used in order that it might acquire the temperature of the tempering bath in the shortest possible time. The test bars were austenitized in their capsules and quenched in water at $+40^{\circ}\text{C}$, the capsules being broken under water. The bars were then further quenched by immersion in liquid nitrogen, from which they were transferred to the dilatometer. The lower end of the dilatometer was then submerged in the tempering bath.

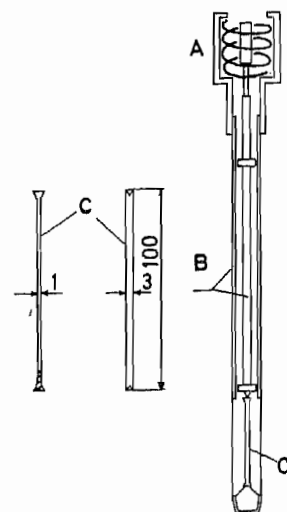


Fig. 8.
Schematic diagram of
the dilatometer.

2.3.2 Carbide separation

The carbides were separated by Modin's [31] method, which had been slightly modified. A solution of 50 % HNO_3 in methanol was used to etch the carbides into relief. The specimen was then washed in the series: water – methanol – methanol – isoamyl acetate. The carbides were finally detached from the surface of the specimen by means of an ultrasonic washing device into a small quantity of isoamyl acetate; upon evaporation of the latter, the carbide powder was left on the bottom of the dish. The specimens tempered at $T_t = 125, 150 \dots 450^{\circ}\text{C}$ were subjected to such carbide separation.

2.3.3 X-ray examinations

The carbides separated in the manner just described were examined by the Debye-Scherrer method. Each examination was made twice, with monochromatic Co and monochromatic Fe radiation, respectively. The carbide particles constituting each sample were usually sprinkled into a narrow capillary to ensure random orientation.

The results obtained by Debye-Scherrer's method were checked by means of diffractometric measurements. The equipment used consisted of an x-ray unit, the diffractometer, a scintillation head with a NaI(Th) crystal, a linear amplifier, discriminator and recorder. Both Mo and Cu tubes were used in the x-ray unit. The radiation passed through a system of slits to reach the

sample. The reflected radiation was admitted by a 0.3 mm receiver slit to the monochromizer and thence to the detector. The reflections were recorded on a chart, from which the glancing angles were read. The sample was prepared by sprinkling carbide particles on a glass plate covered with zapon lacquer.

The changes in amount of retained austenite were measured diffractometrically by the usual method. The face of the planar, heat-treated specimens was levelled by grinding, followed by electrolytic polishing. Diffractometer runs were made on the samples, using monochromatic Co radiation. As calibration, the quantity of retained austenite in a specimen tempered at 220 °C was measured with a linear analyzer. The integrated intensity of the (200) line of austenite was measured from the diffractometer curves and converted to the respective residual austenite quantity with the aid of the calibration data.

The width of the (200) line of martensite and austenite was determined by continuing the straight sides of the peak by hand to intersection with the base line and measuring the intercept.

2.3.4 *Electron microscopy*

Electron microscope observations were made both according to the surface replica and the thin foil method. The replicas were made by the conventional carbon film technique [32] either directly or by the indirect procedure. In the direct procedure, a mixture of C and Pt was evaporated to form a film directly on the surface of the specimen. This film was removed by etching with a 5 % bromine-ethanol etching solution and detached to float on water containing about 2 % HNO₃. After several rinsings, the film was placed on a specimen grid.

For the indirect method, a drop of zapon lacquer was placed on the specimen surface. After drying, the lacquer film was detached and its relief side was coated with an evaporated C-Pt film. The lacquer film was then dissolved in amyl acetate so that the carbon film was left on a specimen grid. The specimens were examined either by a Philips E.M. 100 B or a Siemens Elmiskop I electron microscope.

The thin foils were made according to the method of Glenn and Raley [33], which was slightly modified. The specimen was glued to a supporting block and mechanically reduced to about 0.1 mm thickness. Diamond paste was used in the final stage of mechanical reduction. Glenn and Raley's original method was then followed until the thickness of the specimen was approximately 0.01 mm. A special tool was used to punch from the resulting foil a round which fitted the specimen holder of the electron microscope. The foil was further reduced in thickness in a jig made of Teflon,

employing the above-mentioned electrolytic method. When the first hole appeared, the specimen was removed from the jig, washed and placed in storage in xylene for later microscopy.

The specimen foil was placed in the electron microscope without the specimen grid. By using the described technique, the step of cutting out the sample after the final thinning could be omitted. The punching process caused deformation of the round at its edges, but this caused no trouble because the part of the foil examined was located at the center of the round. The specimens were studied in transmission in a Siemens Elmiskop I with 100 kV accelerating voltage.

2.4 Mechanical testing

2.4.1 Torsion test

The aim of this design was to obtain a testing machine complying with the following requirements, all of which were essential from the viewpoint of the present work:

(a) It should be possible to derive the true stress-true strain diagram from the values recorded in the test by taking account of the test bar dimensions, without need to apply corrections by means of some formula based on certain assumptions. This should apply from the start of deformation up to ultimate fracture of the test specimen.

(b) The testing method should be suitable for fairly brittle substances so that considerable plastic deformation of the test bar would ensue prior to its rupture.

(c) It should be possible to vary the experimental conditions, e.g. the rate of deformation, the testing temperature and the state of stress, within considerable limits.

Comparison of various testing methods revealed that the tensile and compressive strength test and the torsion test with solid test bars conformed poorly to the stated requirements. The torsion test using tubular test bars was found to be most appropriate in the present work.

The tensile test is poorly suited for brittle substances since little plastic deformation occurs prior to rupture [34]. In the case of tough materials, again, the stress state becomes complex immediately when the contraction begins [35].

In the compression test, difficulties are encountered in eliciting the capacity of deformation, because the test does not always result in rupture. Furthermore,

the stress state is complicated by barrelling of the specimen, and the friction between compression anvil and specimen is difficult to estimate [36].

When a solid test bar is subjected to torsion, the stress and strain states vary in its interior according to the distance from the axis of the bar. If only the total angle of twist (φ , in Fig. 9) is taken into account, the result will be indefinite also for the reason that the deformation may be non-uniformly distributed over the neck portion of the test bar [27].

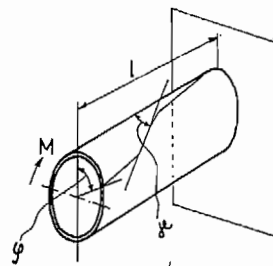


Fig. 9.
Tube subjected to torsion.

The specified requirements are best met by torsion tests with a thin-walled tubular test bar. When the moment M required to produce torsion of the bar and the highest value of the slip angle (γ , in Fig. 9) occurring at each given torque are recorded, the true stress – true strain diagram can be plotted. The shear stress is obtained from the formula

$$\tau = \frac{M}{W} \quad (1)$$

where M stands for the moment and W for the resistance against torsion, while the shearing strain is obtained from the tangent of the slip angle γ . Since the dimensions of the test bar remain essentially unchanged up to the moment of rupture [37], the quotient of moment and stress is constant $= W$, and the state of stress is thus determinable from the moment.

By reason of the rotational motion used to apply torsion, it is a simple matter to adjust the rate at which the test proceeds. The proportion of tensile stress and shear stress can be altered if facilities for applying tension and compression are provided in the testing machine. It is also possible to adjust the temperature of the tubular bar in the test e.g. by passing a fluid of the desired temperature through the bar.

On account of the advantages set forth here, a torsion testing machine suitable for the testing of tubular specimens was designed for use in the present work.

The tubular test bar has to be thin-walled in order that the stress-strain state might be considered constant over its thickness. As a consequence, it tends to buckle when subjected to torsion. Recording of the greatest slip angle also necessitates special arrangements.

A detailed description of the testing machine is to be given in another publication and it will therefore suffice to present it in its main features only.

Fig. 10 gives a general view of the machine. The flywheel mass (C) serves to ensure uniform movement, and acts as a reservoir of energy. Its weight is 350 kp and its moment of inertia, $J = 33 \text{ kgm}^2$. A system of gears has been provided by which the flywheel unit can be made to revolve at any desired speed between 0.001 and 1 400 r.p.m.

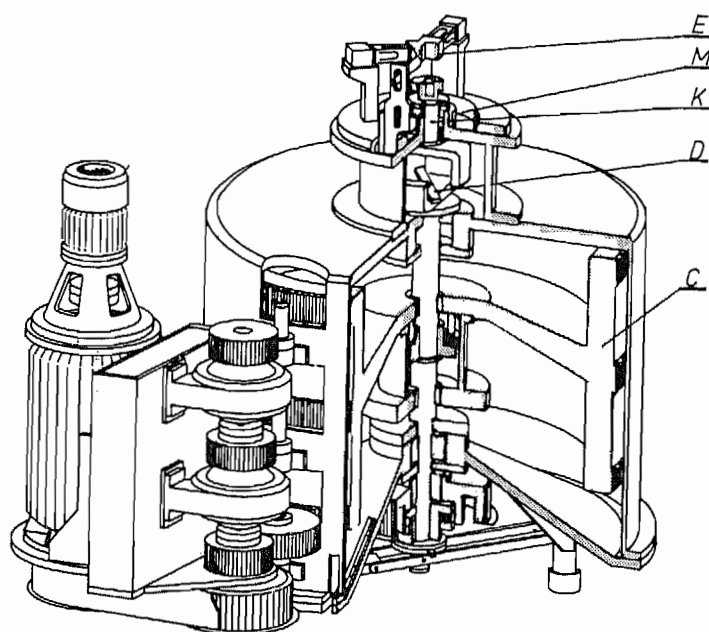


Fig. 10.
Sectional view of the torsion testing machine.

At the beginning of a test, the flywheel is engaged with the end of the test bar by means of a mechanical coupling (D). The sum of the moment resulting from the kinetic energy of the flywheel and of the moment transmitted by the gears from the driving motor turns the lower end of the test bar. The flywheel and driving mechanism were dimensioned so that, according to calculations made in advance, the speed of rotation of the flywheel would suffer a loss of less than 2 % in the course of one test.

The upper end of the test bar is connected to the moment-measuring equipment. This equipment comprises two devices, one for low test speeds (E, in Figs. 10 and 12) and another for high speeds (F, in Figs. 11 and 13). The low-speed moment-measuring attachment was designed to incorporate springs which allow free axial movement of the test bar. This freedom of movement is necessary when the test bar is to be subjected to tensile or

compressive stress during progress of the torsion test. It also enables the test bar to be given various temperatures: the inductive pick-up serving as an electric measuring device is placed at such a distance from the test bar that it is not susceptible to the changes in temperature of the test bar. Measurement of the moment is effected with the aid of a calibrated spring causing a force

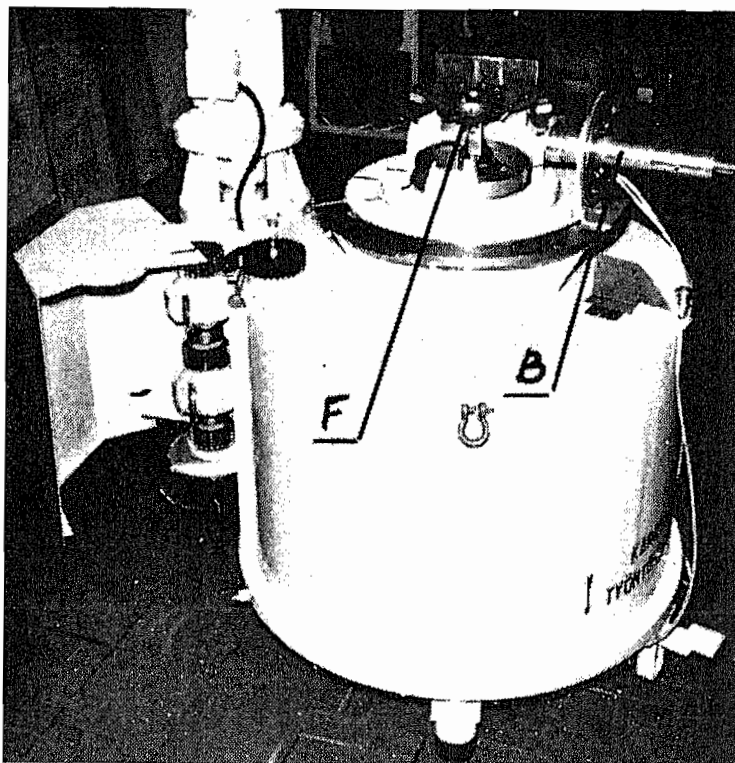


Fig. 11.
The torsion testing machine.

to counteract the moment. An inductive displacement pick-up senses the movements of one end of the spring and gives a signal proportional to the deflection. The electrical signal from the device is transmitted to a recorder.

The high-test speed moment-measuring apparatus was particularly designed to follow rapid changes of moment; its mass was therefore reduced as far as possible. Four short lifting springs are provided as elements serving to measure the moment and four resistance-wire strain gauges cemented to them to furnish a signal proportional to the moment.

The tubular test bars employed in the present work had the shape shown in Figs. 12 and 14. The form of the neck portion apparent from the figures, with its short, straight middle portion and long, gently tapering transition cones which connect to the ends of the bar, was chosen because it was desired to avoid the occurrence of stress peaks and to concentrate the deformation

to the middle portion. The neck portion was ground and polished with diamond paste, and finally with aluminium oxide. The outer diameter and inner diameter of the straight neck portion had to be fixed as a compromise between the machining difficulties and the relative magnitude of the friction forces produced in buckling. As a result of the dimensions chosen on such considerations, the rate of deformation and the amount of deformation are both about 25 % less at the inner than at the outer surface.

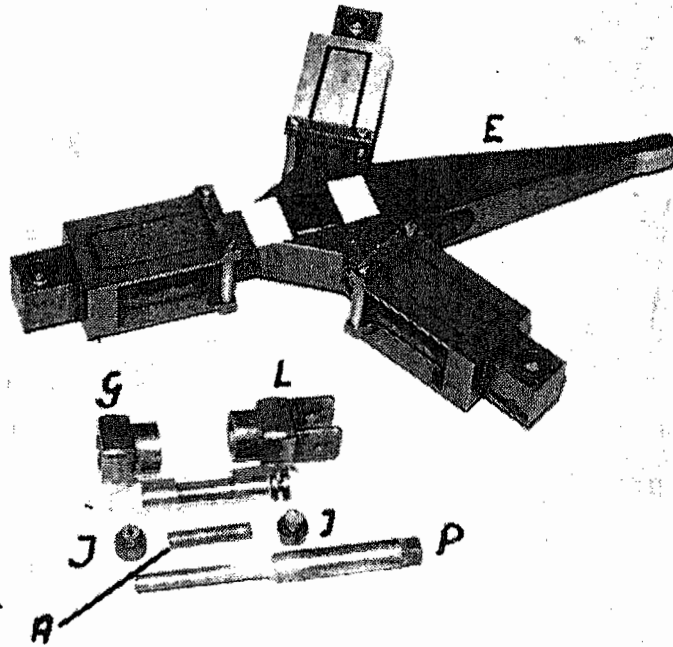


Fig. 12.

The moment-measuring device for low test speeds, and test bar and its attachments.

The test bar was prevented from buckling by insertion of a thick-walled, tubular filling piece (A, in Fig. 12). The magnitude of the lateral force occurring in the event of buckling will depend on the difference in diameter between the test bar and filling piece; the bore of the test bars was therefore honed to a smooth and accurate finish. The insert was hardened steel, ground and electrolytically polished and dimensioned to fit into the bore with about 0.01 mm play. All this was done in order to minimize the lateral force. The friction between test bar and insert caused by the force was reduced by spraying a coat of Teflon on the mating surfaces.

The ends of the test bar were fitted in drivers with spherical surfaces (G and L, in Fig. 12) and with screw clamps (I, in Fig. 12). The drivers were designed to allow free alignment of the test bar: they transmitted only torque and no

bending moments to the bar. In the torsion tests under tensile stress, one of the drivers attached to the test bar is caught in the upper coupling piece of the machine (K, in Fig. 10) in a manner permitting free positioning in the spherical socket.

Tensile stress is produced in the test bar by applying traction to the upper driver (L, in Fig. 12), which has been provided with lugs. The traction was achieved with a lever-and-weight system.

The temperature desired for the test is established in the test bar by conducting a flow of cooling or heating fluid through the bar, for which purpose the lower screw clamp and the filling piece have been axially pierced. The upper screw clamp is replaced in such tests with another clamp having a funnel on top. Fluid poured into the funnel passes through the test bar and flows into an annular receptacle (M, in Fig. 10) surrounding the lower coupling piece, this being ultimately drained by a piece of plastic tubing.

For the purpose of observing the slide angle (γ), a telescope with crosshairs (B, in Fig. 11) was constructed and pivoted so that it was rotatable around its optical axis. The telescope is connected by gear transmission to a precision »Helipot» resistance, from which an electrical signal is obtained, corresponding to the angle through which the telescope is turned. The signal controls a channel of the multi-point recorder which also records the torque signal.

The surface of the test bar, which was placed in a jig, was marked with lines parallel to its axis and spaced at about 1 mm apart (cf. Fig. 32). A line produced with a fine-grained grinding-stone was found to be most appropriate. It caused no notch effect because the surface of the bar was merely dulled, but the line was nevertheless permanent and sharply defined. During the test, the inclination of the lines marked on the bar was followed by the crosshairs of the telescope. The point to be thus observed was chosen on a line opposite the telescope and on the portion of this line where its inclination against the axis of the test bar was greatest.

The method of slip angle measurement just described could be used in tests performed at low speeds. When the tests were performed at higher

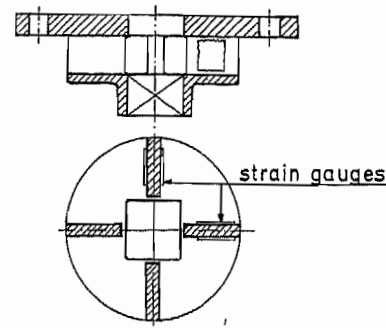


Fig. 13.
The moment-measuring device
for high test speeds.

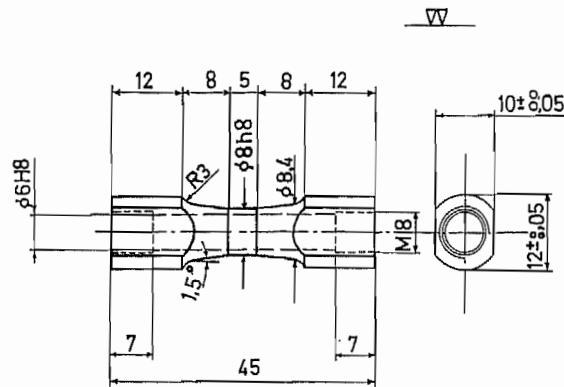


Fig. 14.
The torsion test bar.

speeds, the test bar was photographed with a ciné camera; a time marking device was then used by means of which the film frames could be coordinated with the proper points on the torque curve. For evaluation, the film was projected, frame by frame, to a screen carrying an angle scale, from which the slip angles could be read.

The speed of rotation was recorded with the aid of a magnetic pick-up coil in which a pulsating voltage was generated by the passage of the gear rim on the flywheel. The voltage was recorded so that the exact number of tooth passages making up the total angle of twist could be counted and the angular speed calculated from the value found.

Prior to each test, the speed of rotation was adjusted by trial and error until the number of tooth passages recorded in a given time coincided with the desired value.

2.4.2 Calibrations and checks associated with the torsion tests

Before the actual test series, experiments were undertaken in order to clarify the amount by which the speed of rotation changes on loading. The greatest decrease in speed, about 5 %, was found to occur when the speed of rotation was about 100 r.p.m. The relative loss of speed became less towards lower as well as higher speeds.

In the actual tests the speed of rotation was always recorded. If it was found to have decreased, the average value was used as the speed of rotation.

The moment-measuring system was calibrated with a lever and weights before and after each test series. Calibrations of the angle-measuring system were made at the same frequency by means of a circular division on the gear ring of the telescope.

The friction between the test bar and its filling was studied as follows. The short filling used in the torsion tests was replaced with a long filling piece having a drive square at one end (P, in Fig. 12). This rod was rotated during the test both in the direction in which the test bar was twisted and against it, and the effect of friction was found to be negligible as a rule. Only when the tested bar consisted of very tough material was there a slight increase of the friction moment shortly before rupture; even then its value was less than 0.1 kpm. No account has been taken of friction in the calculations for this reason.

Two different methods were employed in order to keep account of the temperature during the torsion tests. In the tests at the lowest temperature (-110°C), ethyl alcohol cooled with solid CO_2 was allowed to flow along the outer surface of the test bar. The interior of the test bar was cooled with liquid nitrogen until the alcohol on the outer surface was about to freeze.

The testing temperature was then considered to be nearly the solidifying point of alcohol (-110°C). In this manner the alcohol on the outside served as the temperature indicator, while it also prevented rime from forming on the bar, which would have interfered with the slip angle observations.

In the test series at temperatures higher than room temperature, the temperature of the test bar was measured with a small copper-constantan thermocouple tin-soldered to the surface of the bar at its centre. The same arrangement was used in the high-speed tests at room temperature when attempts were made to detect the rise in temperature of the test bar during the test by reason of the deformation. Such measurements were only made with test bars that had been tempered at a temperature considerably exceeding the melting point of the solder.

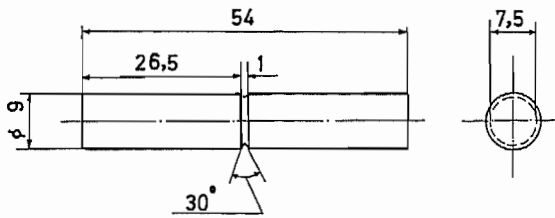


Fig. 15.
The notched-bar impact test bar.

2.4.3 Notched-bar impact test

In the notched-bar impact test a Charpy pendulum and test bars of the shape shown in Fig. 15 were used.

3. RESULTS

The ultimate purpose of the present investigation was to clarify the manner in which the behaviour of martensite under stress depends on the changes in micro-structure occurring on tempering and on the method of material testing. With this in mind, observations were made concerning the effect of tempering on micro-structure and mechanical tests were carried out in which the experimental conditions could be varied. The aim of the observations concerning the deformed structure was to gain information on the deformation process itself.

3.1 Undeformed structure

3.1.1 Dilatometric observations

The changes in length occurring on isothermal tempering of martensite were followed with the aid of the dilatometer (see p. 19). The lowest test temperature was -79°C and the highest temperature was 370°C . The temperatures at which observations were made are almost uniformly distributed over this interval.

In Fig. 16 the relative change in length $\Delta l/l$ has been plotted over the time t_t for different tempering temperatures T_t . The scale of the tempering time axis is logarithmic, starting at 0.5 min. No common origin was used in plotting the different curves each of which has its own starting point. This is because considerable changes in length associated with tempering occur at high temperatures even while the test specimen is being heated up. Since the elongation of the specimen due to its thermal expansion and the change in length associated with tempering processes take place simultaneously, the true starting point could not be recorded. The length of the test specimen in annealed condition was chosen as the initial length l_0 .

Among the graphs representing the relative change in length, that referring to -79°C is notable for its horizontal course. This implies that no tempering processes occur, that is, no precipitation of carbon from solution nor any change of its position in the iron lattice. The -48°C curve already shows

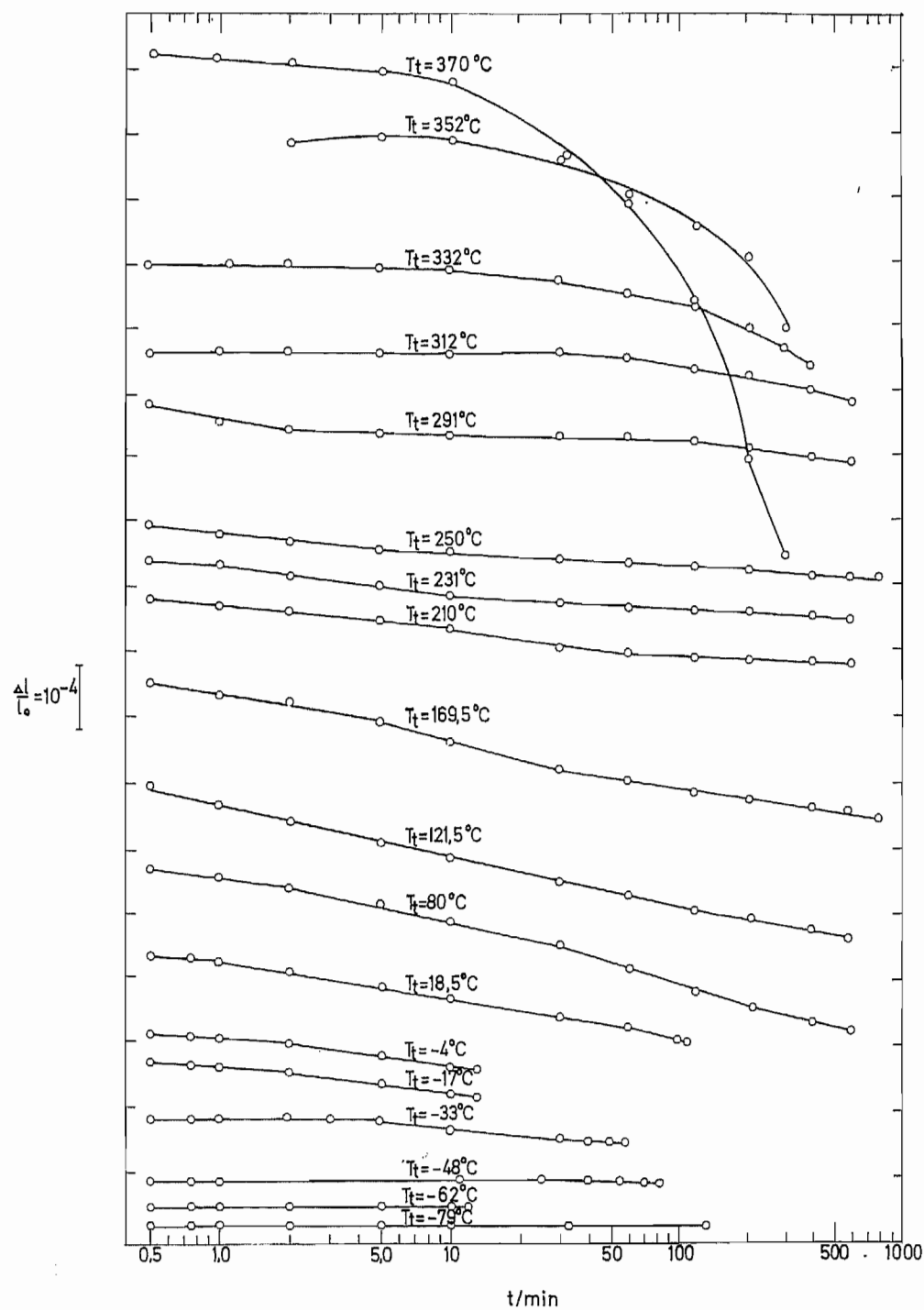


Fig. 16.
Dependence of relative change in length ($\Delta l/l_0$) on tempering time (t) at various tempering temperatures (T_t).

slight decline. Both observations are consistent with earlier reports found in the literature [17].

The graphs corresponding to the tempering temperatures $T_t = -33$ to 291°C are essentially straight lines. At higher temperatures, the graphs become curved, with accelerated decline at their far end. Comparison between Fig. 16 and the results presented by Altstetter et al. [18] reveals distinct conformities.

The course of the graphs obtained for the tempering temperatures $T_t = -79$ to 291°C is largely equivalent to that reported by Altstetter et al., who interpreted the uniform descent of the curves as being associated with the formation of ϵ carbide. The accelerated decline in the latter part of the $T_t = 312$ to 370°C curves was attributed by them to depletion of the matrix of carbon at the formation of cementite.

At the tempering temperatures for which a graph having distinct changes in direction has been obtained, a change in the character of the process can be assumed to take place at a time corresponding to the point of direction change. However, it should be noted that the graphs reproduced in Fig. 16 do

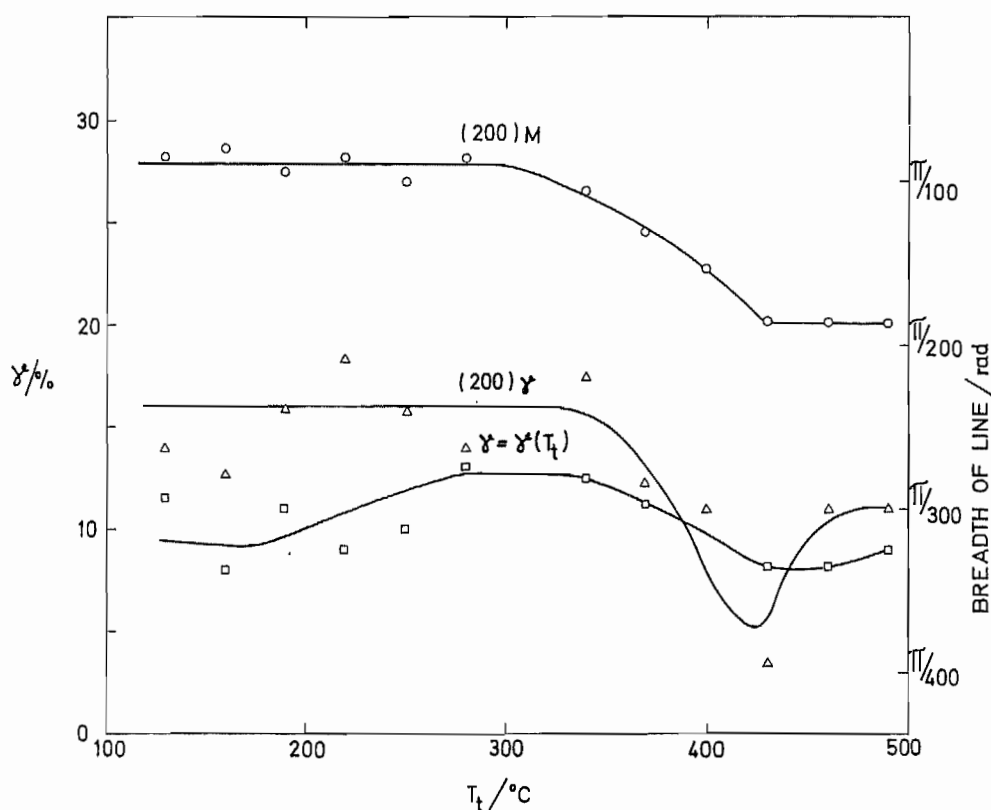


Fig. 17.
Dependence of the amount of retained austenite (γ) and of the martensite (200) and austenite (200) line width on tempering temperature (T_t).

not necessarily reflect merely changes occurring in the martensite: they may also express changes in the quantity of retained austenite. For instance, the portion in the $T_t = 352^\circ\text{C}$ graph showing a definite ascending tendency may be due to the decomposition of retained austenite.

3.1.2 X-ray examinations

In Fig. 17, the amount of retained austenite $\gamma = \gamma(T_t)$ and the width of the martensite $(200)_M$ and austenite $(200)_\gamma$ lines have been plotted against the tempering temperatures. The γ graph representing the amount of retained austenite, $\gamma = \gamma(T_t)$, shows some ascent between the tempering temperatures $T_t = 200$ and 300°C but falls again after 350°C to the 200°C level and even below.

The curves showing the width of the martensite as well as austenite (200) lines decline at temperatures higher than $T_t = 325^\circ\text{C}$. A peculiar feature is the dip in the austenite line width graph around $T_t = 420^\circ\text{C}$.

For the lattice structures of the separated carbides, identical results were obtained within the limits of measuring accuracy, both by Debye-Scherrer's method and with the goniometer, independent of the wavelength employed. Fig. 18 shows the lattice plane spacings (d) determined from the films and records and the visually estimated relative intensities (I) of the corresponding lines. The figure was drawn, for greater ease of comparison, in such a manner that the values corresponding to consecutive tempering temperatures are shown opposite each other, on either side of a horizontal line. The pairs $125^\circ\text{C}/150^\circ\text{C}$, $150^\circ\text{C}/200^\circ\text{C}$, $200^\circ\text{C}/300^\circ\text{C}$ and $300^\circ\text{C}/450^\circ\text{C}$ are thus shown, grouped about their respective horizontals.

Table 2 contains the values found for the spacing of lattice planes (d) at different tempering temperatures. The lattice constants for Fe_2C and Fe_3C

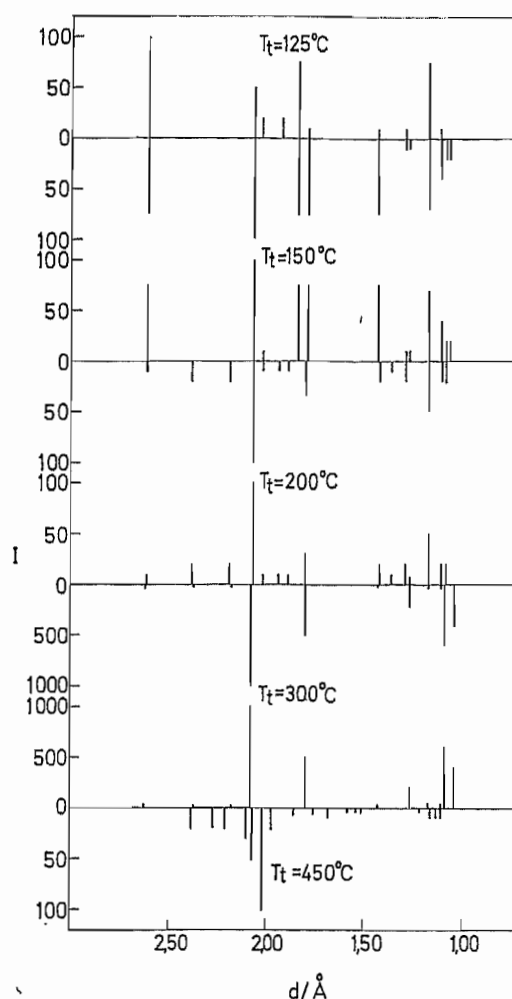


Fig. 18.
Spacing of lattice planes (d) and visually estimated relative intensities (I) of corresponding diffraction lines for the carbides separated from test specimens tempered at various temperatures (T_t).

obtained from the ASTM card have also been entered in the table. The accuracy with which the experimental d values have been stated is slightly excessive: the last figure may not be correct but it is nevertheless thought to be significant.

TABLE 2.

Spacing d of lattice planes (in Å) of the separated carbides corresponding to different tempering temperatures.

| 125 °C | 150 °C | 200 °C | 300 °C | 450 °C | Fe ₂ C ASTM | Fe ₃ C ASTM |
|--------|--------|--------|--------|--------|---------------------------|---------------------------|
| 2.614 | 2.618 | 2.616 | 2.620 | | | 2.38 |
| | | | | | 2.42 | 2.37 |
| | | 2.380 | 2.366 | 2.385 | 2.29 | 2.25 |
| | | | | 2.267 | 2.20 | 2.21 |
| | | 2.187 | 2.183 | 2.210 | 2.18 | 2.10 |
| | | | | 2.102 | 2.13 | 2.06 |
| 2.073 | 2.070 | 2.073 | 2.082 | 2.076 | 2.07 | 2.02 |
| 2.030 | 2.030 | 2.028 | | 2.025 | 2.04 | 2.01 |
| 1.926 | | 1.940 | | 1.975 | 2.02 | 1.97 |
| 1.847 | 1.845 | 1.893 | 1.803 | 1.855 | 2.00 | 1.87 |
| 1.797 | 1.795 | 1.801 | | 1.757 | 1.98 | 1.85 |
| | | | | 1.689 | 1.92 | 1.76 |
| | | | | 1.583 | 1.81 | 1.68 |
| 1.436 | 1.436 | 1.434 | 1.432 | 1.539 | 1.77 | 1.61 |
| | | 1.363 | | 1.512 | 1.73 | 1.58 |
| 1.296 | 1.294 | 1.293 | 1.274 | 1.218 | 1.69 | 1.57 |
| | 1.273 | 1.271 | 1.175 | 1.162 | 1.66 | 1.54 |
| 1.172 | 1.172 | 1.173 | 1.108 | 1.128 | 1.63 | 1.51 |
| 1.107 | 1.108 | 1.107 | | 1.107 | 1.58 | 1.50 |
| | | | | | 1.51 | 1.40 |
| | 1.087 | 1.081 | 1.087 | | 1.48 | 1.35 |
| | | | 1.040 | | 1.43 | 1.34 |
| | | | 0.900 | | 1.38 | 1.32 |
| | | | 0.825 | | 1.34 | 1.29 |
| | | | 0.805 | | 1.28 | 1.25 |
| | | | 0.734 | | 1.25 | 1.22 |
| | | | 0.692 | | 1.22 | 1.21 |

A comparison of the d values found for the carbides produced at the temperatures $T_t = 125, 150$ and 200°C with the values stated in the ASTM card and with those reported by Jack [38], results in fairly good agreement. It is obvious that the ε carbide Fe_2C has an effect. However, it is also clear that considerable deviations exist, which cannot be attributed to inaccuracy in measurement. They may be due to the alloying constituents of the steel used.

Very good agreement between the d values found for the carbides produced at a tempering temperature of $T_t = 450^\circ\text{C}$ with those stated for cementite in the ASTM card is evident. Cementite is certainly responsible here. The carbides obtained in the tempering temperature region $T_t = 250$ to 375°C yielded x-ray patterns differing from the others in appearance. As can be seen from Fig. 18, only a few really strong lines are visible. In parallel tests carried out on a steel having a composition identical to that of the steel used in this work, except for the absence of silicon, the same strongly defined lines were observed. The sole difference is that the lines clearly identifiable as cementite lines appeared in the film taken of the carbides produced at $T_t = 325^\circ\text{C}$, while in the case of the steel proper of this work they appeared when the tempering temperature was $T_t = 375^\circ\text{C}$.

The fit of the d values found for the carbides produced at $T_t = 300^\circ\text{C}$ with the cementite d values is poor. This is clearly realized if one compares the $1/d^2$ values calculated from the data $a = 4.517 \text{ \AA}$, $b = 5.079 \text{ \AA}$, $c = 6.370 \text{ \AA}$ stated for cementite in the ASTM card with the $1/d^2$ values of the said carbides. Calculating the difference of the closest pair of values,

$$\Delta \frac{1}{d^2} = \frac{1}{d_{\text{obs}}^2} - \frac{1}{d_{\text{calc}}^2} \quad (2)$$

we find that nearly all deviations exceed the estimated limit of error, $\pm 0.002 \frac{1}{\text{\AA}^2}$ (Fig. 19). They show no systematic trend that might be attributed to any effect from the alloying elements.

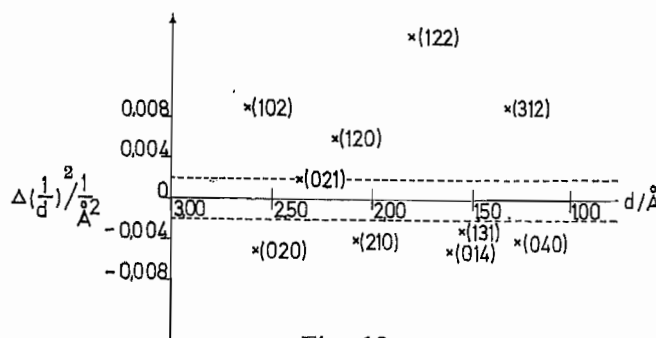


Fig. 19.

Difference $\Delta \frac{1}{d^2}$ of the $\frac{1}{d^2}$ value of the carbides produced at tempering temperature $T_t = 300^\circ\text{C}$ and the $\frac{1}{d^2}$ value of cementite at different values of d , and error limits of measurement.

It would thus seem that the carbide produced in the tempering temperature range $T_t = 225$ to 400°C is not cementite. On the other hand, certain points of agreement can be noted between the d values of the carbides produced at $T_t = 300^\circ\text{C}$ and those of the carbides obtained at lower temperatures. However, part of the lines of the lower-temperature carbides have vanished, while new, fairly strong lines have appeared ($d = 1.087 \text{ \AA}$, and $d = 1.040 \text{ \AA}$). Moreover, the intensities and their proportions are entirely different: several lines almost equal in intensity were obtained with the carbides produced at $T_t = 125^\circ\text{C}$ and especially with those produced at $T_t = 150^\circ\text{C}$, whereas only one powerful line is noted for $T_t = 200^\circ\text{C}$. When the tempering temperature had been $T_t = 150^\circ\text{C}$ and 200°C , the region around the line $d = 2.07 \text{ \AA}$ was somewhat diffuse, a condition which was not observed with any other tempering temperature. For $T_t = 300^\circ\text{C}$, the intensity of the line in question was about ten times that of the corresponding line obtained after tempering at lower temperatures.

Certain anomaly in the lines of carbides produced at different tempering temperatures has previously been observed e.g. by K u r d j u m o w [19]. He investigated a steel having an analysis very different from that of the present work and arrived at the conclusion that an effect caused by the form factor of platelike cementite precipitates could be responsible. The Russian literature also contains information, mainly gained by coercive measurements, concerning intermediate carbides between ϵ carbide and cementite, which the Russian authors refer to as Fe_xC [39]. Any relationship between the anomaly noted in the present work at the tempering temperature $T_t = 300^\circ\text{C}$ with that reported by the Russians is difficult to ascertain.

Since a degree of conformity exists between the d values of the carbides produced in the tempering temperature range $T_t = 225$ to 300°C and those of the carbides obtained at the lower temperatures, it has to be considered possible that ϵ carbide or some carbide closely related to it could be responsible. It is also possible that retained austenite accompanying the separated carbide particles as an impurity causes the effect in question.

3.1.3 *Electron microscopy*

Observations with the electron microscope were made on the test specimens tempered at $T_t = 310$, 390 and 430°C .

Fig. 20 shows a surface replica picture of a specimen tempered at $T_t = 310^\circ\text{C}$, while a thin foil picture of the same specimen is seen in Fig. 21. The first-mentioned displays martensite lenses containing platelike carbide precipitates (K), and areas of retained austenite (γ). The location of the platelike

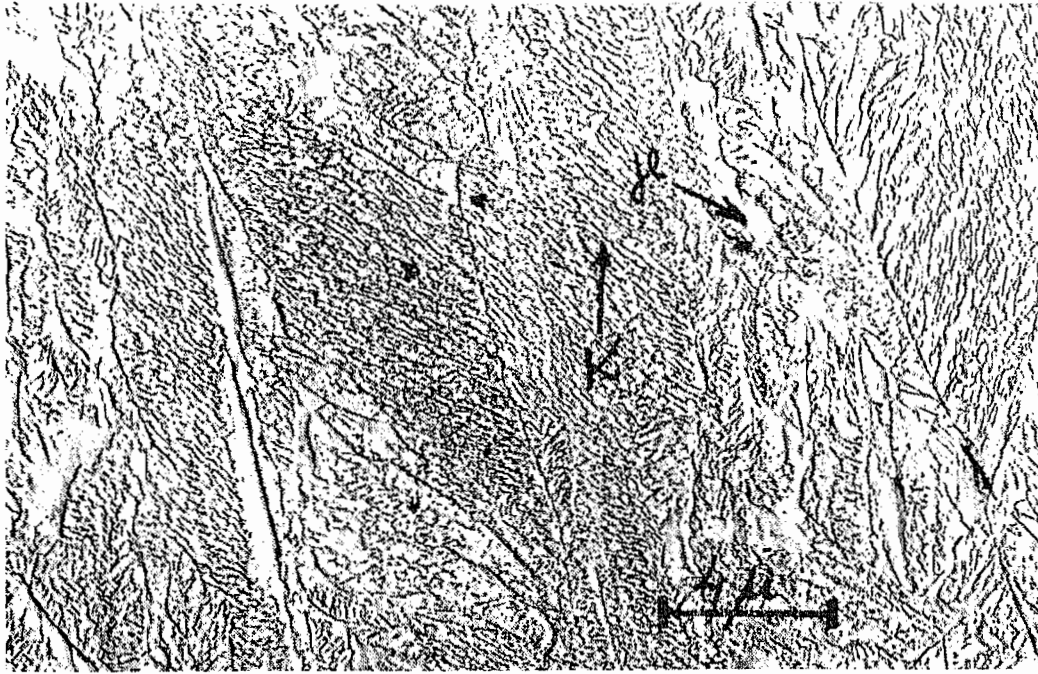


Fig. 20.
Martensite lenses containing platelike carbide precipitates (K), and areas of retained austenite (γ); $T_t = 310^\circ\text{C}$. (Surface replica electron micrograph.)



Fig. 21.
Platelike carbide precipitates in martensite lenses; $T_t = 310^\circ\text{C}$ (Thin foil electron micrograph.)



Fig. 22.
Spherical carbide precipitates in martensite; $T_t = 390^\circ\text{C}$. (Surface replica electron micrograph.)

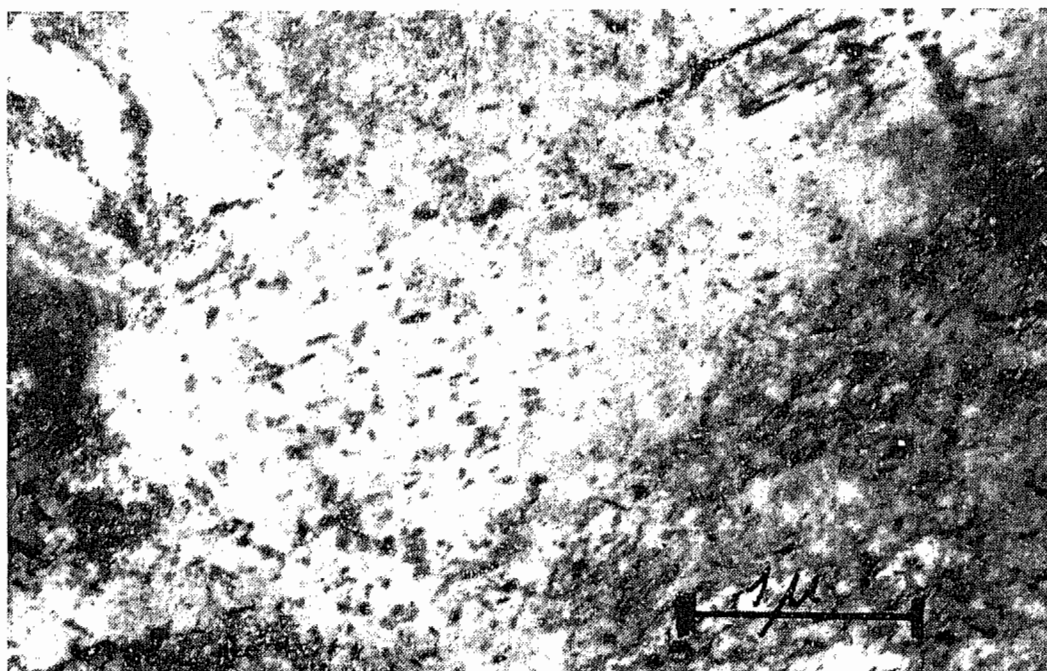


Fig. 23.
Spherical carbide precipitates in martensite; $T_t = 390^\circ\text{C}$. (Thin foil electron micrograph.)

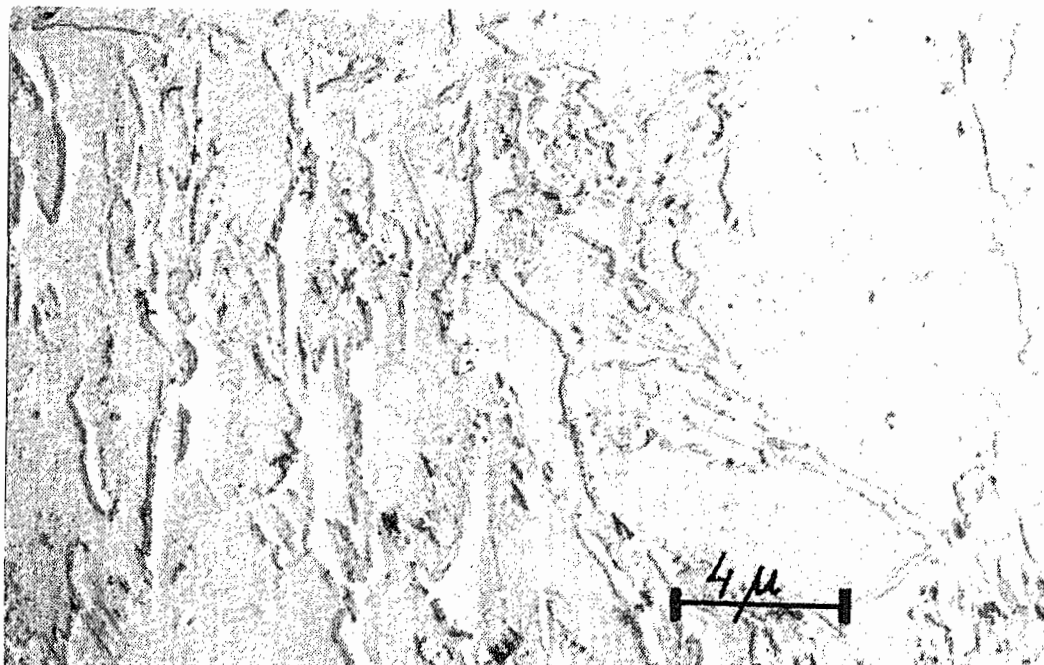


Fig. 24.
Precipitates joined into ribbons; $T_t = 430^\circ\text{C}$. (Surface replica electron micrograph.)

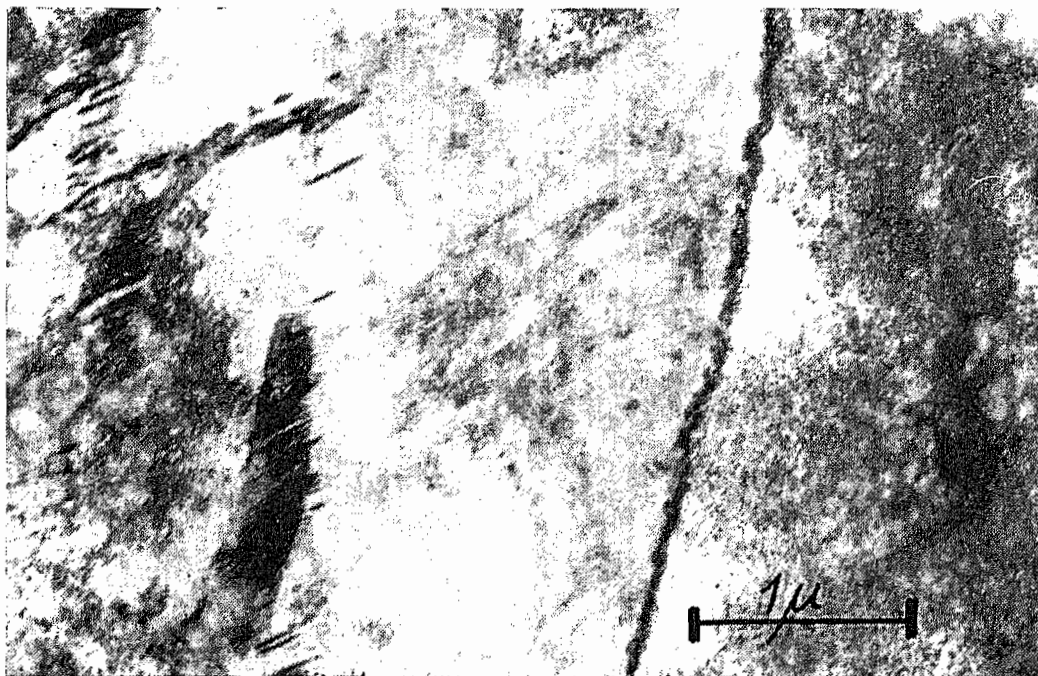


Fig. 25.
Precipitates joined into ribbons; $T_t = 430^\circ\text{C}$. (Thin foil electron micrograph.)

precipitates is not quite regular; at least two separate systems may occur within one martensite lens. Similar observations were also made on examination of some thin foils. In certain instances, precipitate plates belonging to two different systems could even occur at one and the same place. The angle between the orientations of the systems was 60 degrees. Such criss-cross growth was less frequent, however, than parallel orientation of the kind seen in Fig. 21. Comparison between Figs. 20 and 21 with previously published micrographs [27] shows obvious similarities.

The surface replica and thin foil electron micrographs reproduced in Fig. 22 and 23 respectively were derived from a specimen tempered at $T_t = 390^\circ\text{C}$. It can be seen that the platelike precipitates have disappeared and are replaced by spherical precipitates. Such spherical formation was found to occur within a fairly narrow temperature range, incipient signs of the phenomenon being observable already when the tempering temperature had been $T_t = 370^\circ\text{C}$.

A specimen tempered at $T_t = 430^\circ\text{C}$ is illustrated in the surface replica and thin foil electron micrographs in Fig. 24 and 25, respectively. The figures reveal that the precipitates have joined to form ribbons, part of which may be found in the boundary area between regions of retained austenite and martensite lenses. Some tendency towards such localization can already be seen in Fig. 22 (κ).

It was noted in the observations with the electron microscope that in the specimen tempered at 390°C recovery of the matrix had taken place, resulting in some resolution of the dislocation tangles. The fact that dislocations were actually concerned was demonstrated by their movement which occurred when the electron beam was allowed to cause heating of the area under investigation. The dislocations moved in groups, not singly. No such movement could be elicited in specimens tempered at lower temperatures. This is thought to be attributable to the anchoring effect both of the precipitates and of the carbon in solution at the lower temperatures.

3.2 Mechanical tests

3.2.1 Torsion tests at various speeds

Torsion tests were carried out at nine different speeds of rotation. The lowest speed was $n = 0.00137$ r.p.m. and the highest speed, $n = 640$ r.p.m. The intermediate testing speeds were chosen to form an approximately equidistant series on a logarithmic scale. The tests were carried out at room temperature.

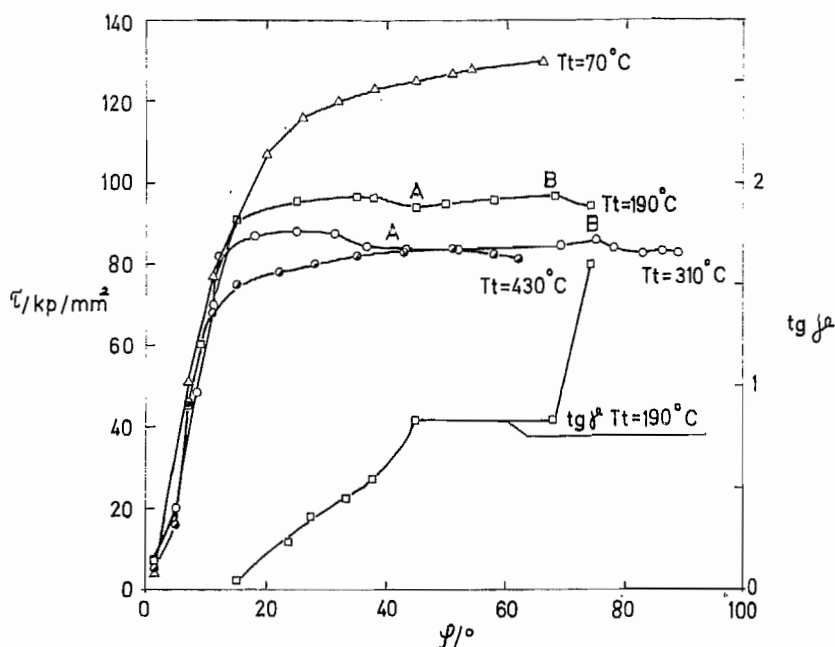


Fig. 26.
Shear stress—total twist (τ/φ) curves obtained at a speed of rotation of $n = 42.6$ r.p.m. Testing temperature $T_k = 25^\circ\text{C}$.

The measuring equipment connected with the testing machine immediately yielded the shear stress (τ) as a function of the total twist (φ). Fig. 26 shows the curves representing this relationship of shear stress and total twist, which shall be called the τ/φ curves. In the same diagram the shear strain $\text{tg } \gamma$, found in the manner described in section 2.4.1, has been plotted by way of an example. On the basis of such graphs, the equivalent shear stress—shear strain curves have been drawn. They shall be designated $\tau/\text{tg } \gamma$ curves, and the results of the torsion tests will be mainly presented in terms of such curves.

Tests have been carried out with test bars tempered at $T_t = 70, 190, 310$ and 430°C . Their results are presented in Figs. 26—31. Fig. 27 contains the $\tau/\text{tg } \gamma$ curves obtained at low speeds, Fig. 28 those found at medium speeds, and Fig. 29 the corresponding curves for high test speeds.

Low speeds. The $\tau/\text{tg } \gamma$ curves in Fig. 27 are seen to group themselves according to the tempering temperature. The spacing between adjacent families of curves is about 10 kp/mm^2 . Within one group, only the curves corresponding to the tempering temperature $T_t = 430^\circ\text{C}$ deviate from each other in such an amount that this can be assumed to be due to the change in speed of rotation (n) in the test. The deviations in any other group may be attributed to random scattering. The curves representing the tempering temperatures $T_t = 190$ and 430°C ascend at a higher rate than the corre-

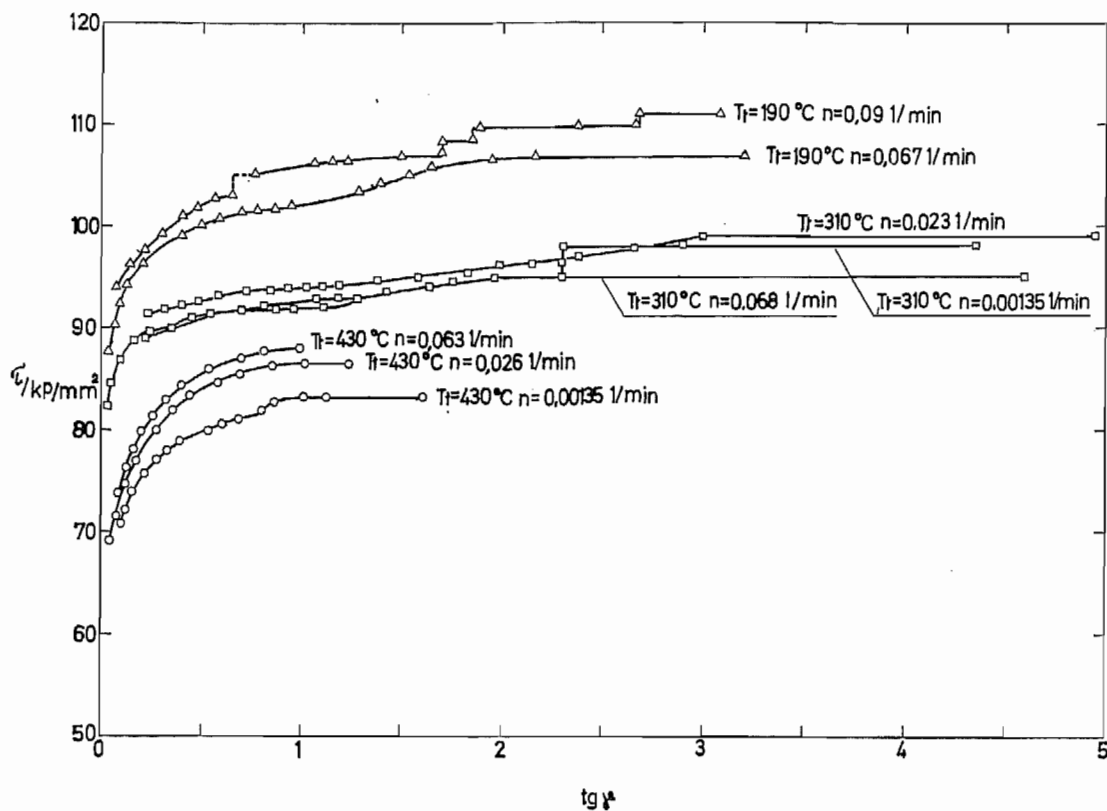


Fig. 27.

Shear stress—shear strain ($\tau/\text{tg}\gamma$) curves obtained at low speeds of rotation. Testing temperature $T_k = 25^\circ\text{C}$.

sponding curves for $T_t = 310^\circ\text{C}$, but the rise continues up to very high values of $\text{tg}\gamma$ in the latter.

It is typical of the curves corresponding to $T_t = 190$ and 310°C that their rate of inclination first diminishes, but later increases and then ultimately diminishes to approach zero. The same course is also encountered in the curve obtained for $T_t = 430^\circ\text{C}$ at a speed of $n = 0.00135$ r.p.m. At certain values of $\text{tg}\gamma$ the ascent may indeed become vertical, as exemplified by the curve corresponding to $T_t = 310^\circ\text{C}$ and $n = 0.00135$ r.p.m.

Increase in the rate of rise of the $\tau/\text{tg}\gamma$ curve implies slowing-down of the deformation; vertical ascent indicates its complete cessation at the γ maxima. When the angle of inclination is 90 degrees, the total twist increases by reason of widening of the deformed region in the neck portion of the test bar. At the same time the stress increases although γ remains unchanged. As soon as the stress has sufficiently increased either during slow deformation or after the deformation has completely stopped, the deformation will again continue in a narrow deformation band, without further increase of stress. The narrow band widens and at this time no other deformation is seen. At the com-

mencement of a test, the deformation never starts in this pulsating manner; on the contrary, it is characterized by wide extent and steady progress. Pulsation only begins when a considerable amount of deformation has taken place, and it never occurs in the specimens tempered at $T_t = 430^\circ\text{C}$. Similar observations revealing pulsating progress of deformation have been made before [27, 40].

The test bar fails by fracture at right angles to the longitudinal axis. The fracture initiates in the deformation band at a point where the deformation has been particularly extensive, i.e., where γ has been high.

Medium speeds. The $\tau/\text{tg}\gamma$ curves obtained at medium speeds (Fig. 28) are different from those which resulted from the tests at low speed (Fig. 27). The increase in speed of rotation has caused a downward shift of the families of curves. This effect of the speed of rotation is also notable within each group.

At the speed of $n = 4.23$ r.p.m., the curve corresponding to $T_t = 310^\circ\text{C}$ has acquired a horizontal initial portion. Already the curve for $n = 0.56$ r.p.m.

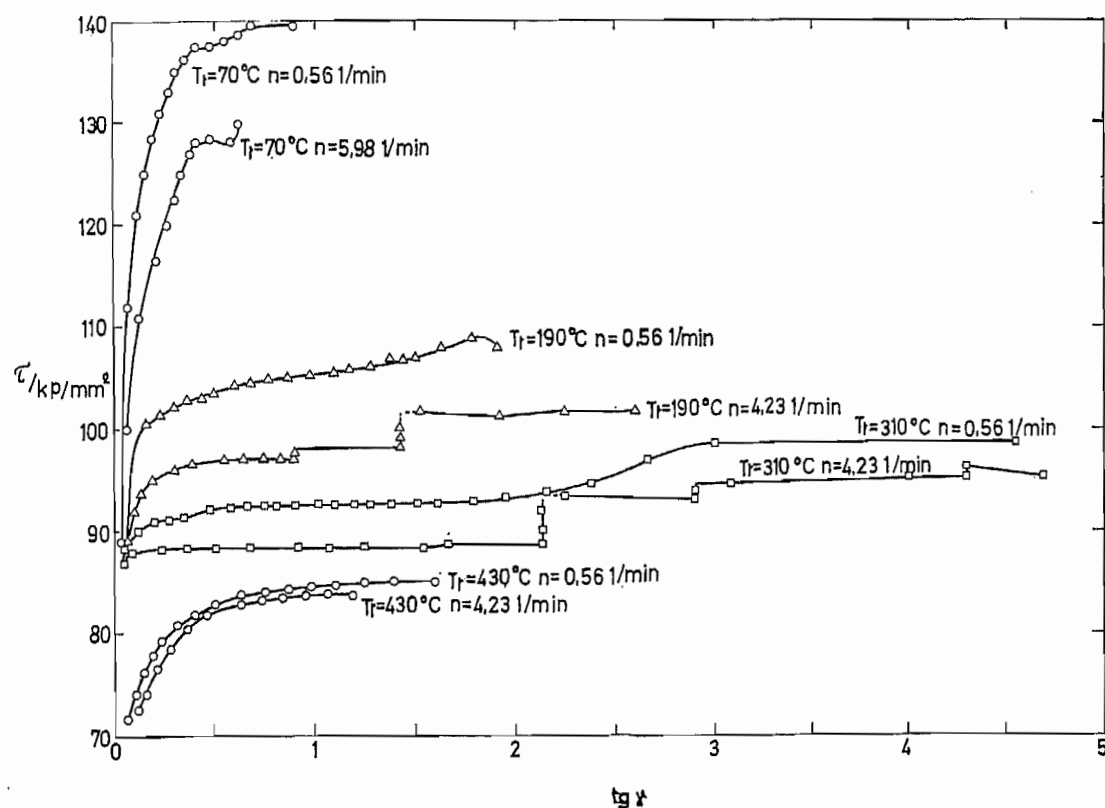


Fig. 28.
Shear stress - shear strain ($\tau/\text{tg}\gamma$) curves obtained at medium speeds of rotation. Testing temperature $T_k = 25^\circ\text{C}$.

and for the same tempering temperature is nearly identical in appearance. The inclination of the curve in the deformation range of about $\text{tg} \gamma = 2.5$ is steep in both instances.

The curves corresponding to $T_t = 70^\circ\text{C}$ rise at a steep rate. They, too, change direction in their later portions, and these modifications are actually accompanied by a decrease in stress.

H i g h s p e e d s. The $\tau/\text{tg} \gamma$ curves obtained at high testing speeds (Fig. 29) differ essentially from those which were derived from tests at low or medium speeds of rotation (Figs. 27 and 28). The curves corresponding to the tempering temperatures $T_t = 190, 310$ and 430°C have been shifted farther down, and their initial ascent has steepened. It is particularly to be noted that the curves descend after a certain deformation, which implies that work-softening occurs in the test specimen.

The anomalies present at high speeds were already evident in the τ/φ curves. It can be seen from Fig. 26 that τ undergoes undulating fluctuations with increasing φ in those cases in which the tempering temperature was $T_t = 190$ and 310°C . This fluctuation is accompanied by a definite sound

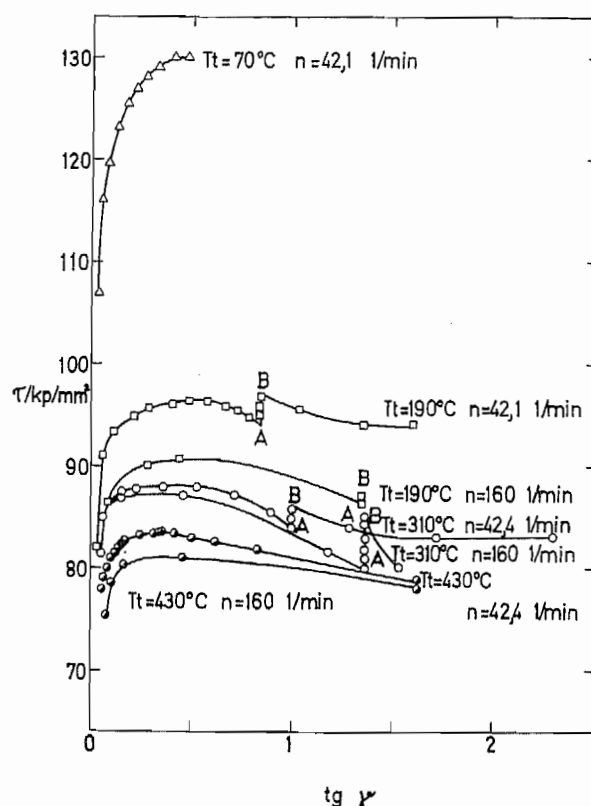


Fig. 29.
Shear stress-shear strain ($\tau/\text{tg} \gamma$) curves obtained at high speeds of rotation. Testing temperature $T_k = 25^\circ\text{C}$.

quite audible in the testing machine. Similar, yet much slighter undulation could already be observed in the tests in which the speed of rotation was $n = 4.23$ r.p.m. A great number of waves was recorded in that instance.

It should be pointed out in respect of comparison of Figs. 26 and 29 that the intervals A–B correspond to each other. As was previously observed in discussing Fig. 27, upward shift between A and B was equivalent to increase in width of the deformation band.

At a speed of $n = 42.1$ r.p.m., the τ/φ curve developed two waves when the tempering temperature was $T_t = 190$ and 310°C . At a speed of $n = 160$ r.p.m., fracture occurred already after the first wave in the test bar tempered at $T_t = 190^\circ\text{C}$, and consequently only a short stump of the $\tau/\text{tg}\gamma$ curve, A–B, was generated (Fig. 29). However, distinct waves were still formed in the τ/φ curve corresponding to $n = 160$ r.p.m. and $T_t = 310^\circ\text{C}$, and the $\tau/\text{tg}\gamma$ curve accordingly shows a distinct rise A–B (Fig. 29).

At the speed of $n = 320$ r.p.m. and still at $n = 640$ r.p.m., the curves corresponding both to $T_t = 190^\circ\text{C}$ and 310°C display the first swing and an equivalent, short vestige of the rise A–B. In the curves corresponding to $T_t = 70^\circ\text{C}$ and 430°C no ascending portion was observable after the first swing, although a distinct falling portion could be discerned in the τ/φ curves just prior to the moment of fracture.

Fracturing total twist—rotation speed (φ_{fr}/n) curve. Immediate observations on the testing machine enabled the total twist (φ_{fr}) preceding fracture to be measured at different speeds of rotation (n). The results obtained in this respect have been compiled in Fig. 30, in which φ_{fr} has been plotted over $\log n$ separately for the test specimens tempered at each of the temperatures $T_t = 70, 190, 310$ and 430°C . The φ_{fr}/n graphs are straight lines with jumps in level, except in the curve for $T_t = 430^\circ\text{C}$.

At the tempering temperature $T_t = 70^\circ\text{C}$, the curve representing the fracturing total twist φ_{fr} jumps upward between the speeds of $n = 0.1$ and 1.0 r.p.m. and declines with increase in speed after this jump.

In the φ_{fr}/n curve consistent with $T_t = 190^\circ\text{C}$ a downward jump occurs in the speed interval $n = 10 - 100$ r.p.m. Before this jump, the graph climbs with increasing speed (n), whereas it assumes a falling tendency after the jump. In the transition range, in the case indicated with B, two swings of the τ/φ curve were obtained (Fig. 26). The total twist consistent with the first swing has been denoted with B'.

At the tempering temperature $T_t = 310^\circ\text{C}$, the rise of the φ_{fr}/n line continues at least up to $n = 4.26$ r.p.m. After that comes a downward jump, followed by descent of the line. The points A and C in the interval of the jump were derived from tests which produced two swings in the τ/φ curve (Fig. 26). The total twists consistent with the first swing have been marked with A' and C'. The experimental points indicated with primes are located on the

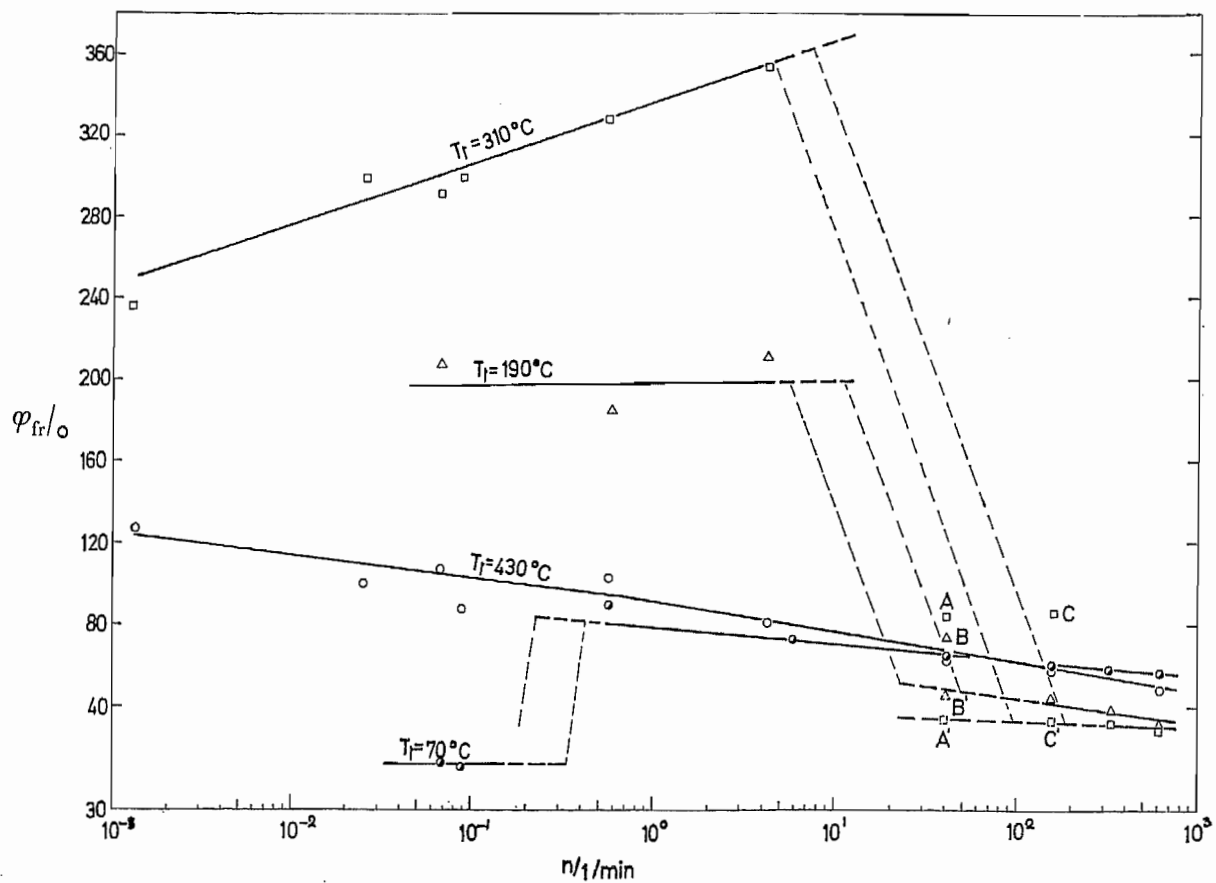


Fig. 30.

Fracturing total twist – speed of rotation (φ_{fr}/n) curves consistent with various tempering temperatures (T_t). Testing temperature $T_k = 25^\circ\text{C}$.

continuation of the straight line drawn through the points obtained with higher speeds of rotation. This clearly shows that only one wave occurred at speeds above the jump.

When the tempering temperature is $T_t = 430^\circ\text{C}$, the φ_{fr}/n curve declines uniformly within the investigated range of speeds.

Local shear strain – length ($\text{tg}\gamma_1/l$) curve. When the values of the local shear strain $\text{tg}\gamma_1$ indicating the strength of plastic deformation were measured at different points on the neck portion of the fractured test bars and plotted over the position in axial direction, the group of curves reproduced in Fig. 31 was obtained. The graph for each test bar has been given its own zero point in drawing these curves. The $\text{tg}\gamma_1/l$ curves for one and the same tempering temperature have been placed one below the other so that the speed of rotation increases from top to bottom. The

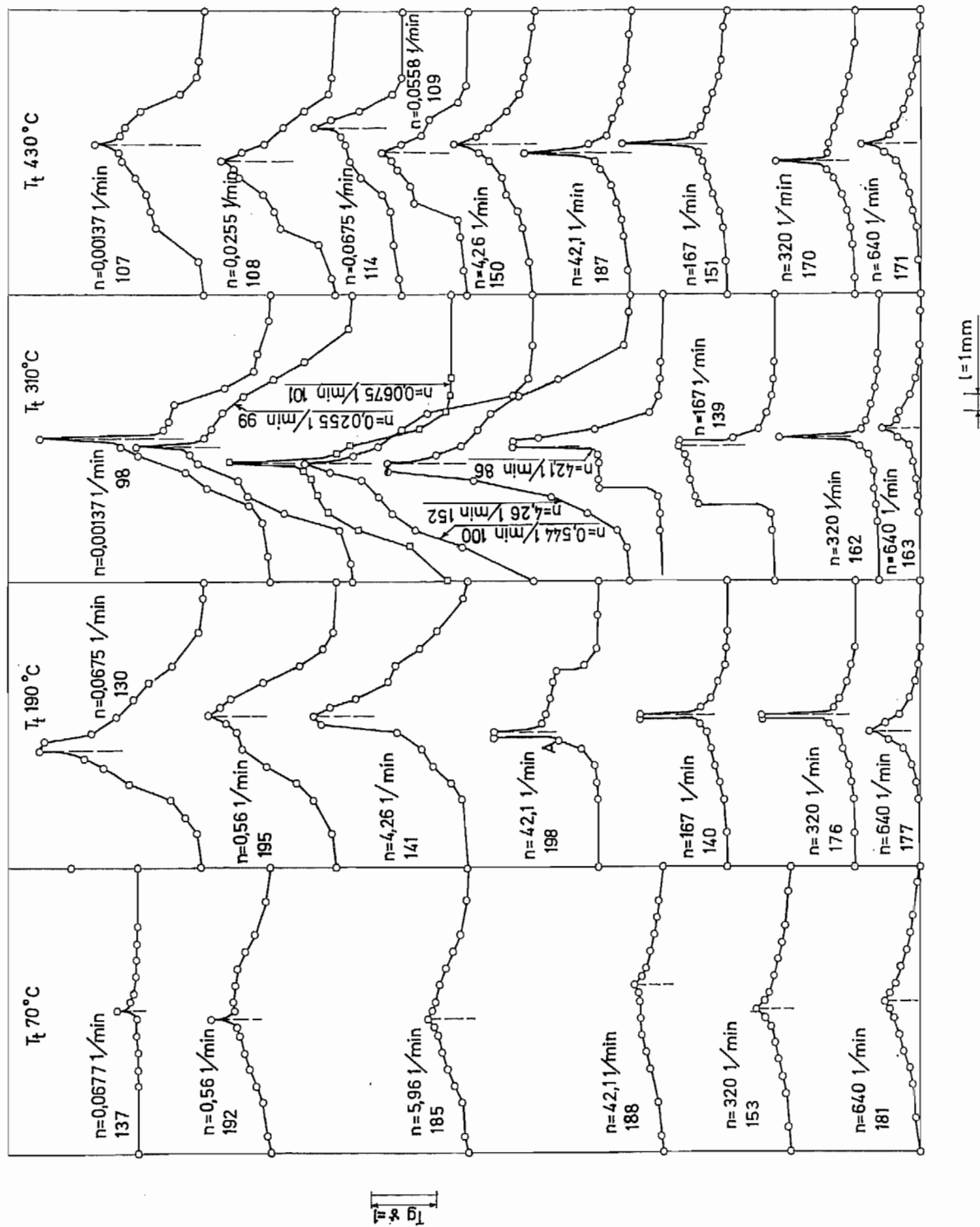


Fig. 31.

Local shear strain - length ($\text{tg}\gamma_1/l$) curves for various tempering temperatures (T_t) and speeds of rotation (n). Testing temperature $T_k = 25^\circ\text{C}$. Value on n and number of test bar inscribed beside each curve.

speed has been inscribed beside each curve, and the point of fracture has been indicated with a dotted vertical line.

At the tempering temperature $T_t = 70^\circ\text{C}$, the graphs are rather shallow, with only a small peak around the point of fracture. At small speeds of rotation, i.e., before the jump in the φ_{fr}/n curve (Fig. 30), the fracture was caused by the tensile stress [40], while fracture by shearing occurred at 0.56 r.p.m. and higher speeds [41].

The $\text{tg}\gamma_1/l$ curves obtained with test bars tempered at $T_t = 190^\circ\text{C}$ are fairly regular up to $n = 4.26$ r.p.m., rising to a ridge at the point of fracture. The curve consistent with $n = 42.1$ r.p.m. is exceptional in that it has two regions of constant $\text{tg}\gamma_1$. The fracture occurred on the boundary between the two regions. The film taken during the test reveals that the test bar suffered, at first, a fairly uniformly distributed twist, whereupon the deformation concentrated to a band. A narrow, yet not sharply demarcated band was formed, in which the deformation $\text{tg}\gamma$ was equivalent to the value A in Fig. 31, No. 198, and in Figs. 26 and 29. The band increased in width, forming the lower deformation level range in Fig. 31, No. 198. The widening band figuratively ate into the surrounding, pre-deformed area with the final result that the band was sharply limited against areas in which the deformation remained small. In the phase of progressive widening, the stress rose to the levels indicated with B in Figs. 26 and 29. After that, a new, narrow band was formed in the widened zone, corresponding to the upper deformation level band in Fig. 31, No. 198. At the same time, the stress (τ) decreased, following the τ/φ and $\tau/\text{tg}\gamma$ curves in Figs. 26 and 29, from B onward. The

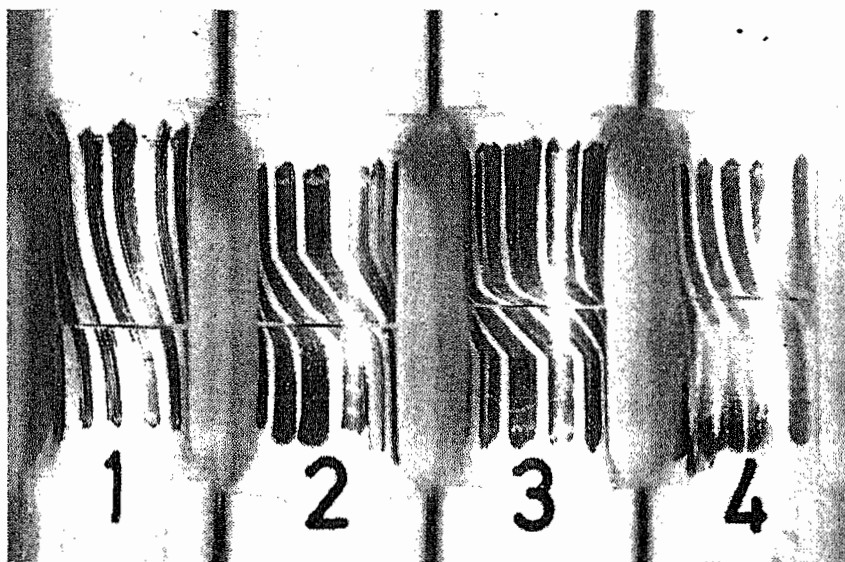


Fig. 32.

Test specimens subjected to torsion at $n = 42.1$ r.p.m. after tempering at $T_t = 70^\circ\text{C}$ (1), 190°C (2), 310°C (3) and 430°C (4). Testing temperature $T_k = 25^\circ\text{C}$. Magnification $2\times$.

neck portion of the test bar in which the deformation phenomenon took the course just described is shown by the enlarged photograph, Fig. 32.

At speeds of rotation higher than the above-mentioned, $n = 42.1$ r.p.m., only one coherent band was formed on the test bar, and which appears in the $\text{tg}\gamma_1/l$ curve of Fig. 31 as a flat-topped peak. This peak remained rather insignificant at $n = 640$ r.p.m.

Examination of the $\text{tg}\gamma_1/l$ curves corresponding to $T_t = 310^\circ\text{C}$ (Fig. 31) reveals that the distribution of deformation at low test speeds was very closely the same as at the tempering temperature $T_t = 190^\circ\text{C}$. The sole difference consists of an area presenting a peak, around the point of fracture. With increasing speed of rotation, the $\text{tg}\gamma_1/l$ curves change in the same manner as with $T_t = 190^\circ\text{C}$, differing only in that the system of bands which was formed in the test bars tempered at $T_t = 190^\circ\text{C}$ when the speed was $n = 42.1$ r.p.m., now also appeared at the speed of rotation $n = 167$ r.p.m. Otherwise, the systems of bands developed in the same manner in both instances.

After tempering at $T_t = 430^\circ\text{C}$, the $\text{tg}\gamma_1/l$ curves obtained at low speeds were rather flat, with merely a small peak at the point of fracture. The peak grew in height with increasing speed, but the value of $\text{tg}\gamma_1$ in the adjacent areas became correspondingly smaller.

Measurements of the heat produced in the test bar were made in the tests in which the speed of rotation was $n = 160$ r.p.m. Successful accomplishment of this measurement proved to be quite difficult in practice, but rises in temperature about 70°C in magnitude could be positively observed.

3.2.2 Torsion tests at various temperatures

In the experiments concerning the influence of testing temperature on the results of the torsion test, the speed of rotation was kept constant at $n = 0.074$ r.p.m. The following testing temperatures were chosen: $T_k = -110^\circ\text{C}$, about $+22^\circ\text{C}$, and $+95^\circ\text{C}$.

At the lowest testing temperature, -110°C , untempered test bars were used, which were considered to have been »tempered» at $T_t = -110^\circ\text{C}$; in addition, specimens tempered at $T_t = 27, 60, 191, 310$ and 430°C were subjected to torsion tests at this temperature. Equivalent series of specimens were tested at the other two temperatures mentioned above, omitting specimens with a tempering temperature lower than the testing temperature.

Tests at -110°C . The results from the tests carried out at -110°C can be seen in Figs. 33 and 34. Fig. 33 presents the graphs produced by the testing machine recorder, which represent the shear stress (τ) as a function of the total twist (φ).

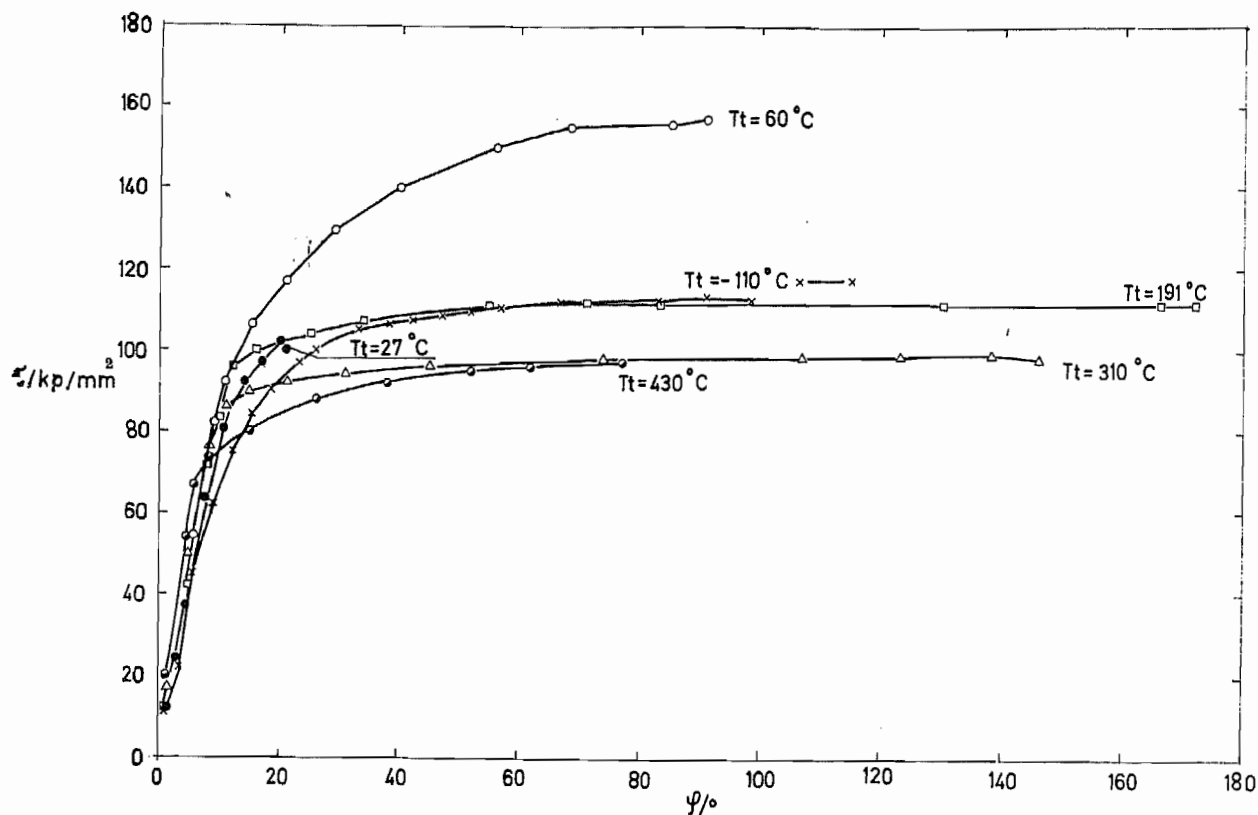


Fig. 33.

Shear stress-total twist (τ/φ) curves obtained at a testing temperature of $T_k = -110^\circ\text{C}$. Speed of rotation $n = 0.074$ r.p.m.

With untempered martensite, yielding starts at a fairly low stress and the τ/φ curve is strongly inclined from its very start. It assumes nearly horizontal course without any clearly marked turning point.

The τ/φ curve found for the specimen tempered at $T_t = 27^\circ\text{C}$ rises at a higher rate than the preceding curve, and fracture occurred at a small value of the total twist. At the tempering temperature $T_t = 60^\circ\text{C}$, the curve is seen to rise to considerably higher level than any other curve, and its curvature continues up to the point of rupture. The curves corresponding to $T_t = 191$ and 310°C display a fairly distinct angulation: their subsequent course is nearly horizontal and continues up to high total twist values. A distinct turn in direction also appears in the curve for $T_t = 430^\circ\text{C}$, but a fairly steep rise persists even after that.

The significant observation can be made on comparison of the different τ/φ curves that the curves derived from specimens tempered at low or moderate temperatures present a curved course without angulation, whereas a distinct knee is seen when the specimen is tempered at $T_t = 191, 310$ or 430°C . It would further seem that the modulus of rigidity G , which is represented by the angle of ascent of the τ/φ curve, increases with increasing tempering temperature.

The stress-strain diagrams, i.e. the $\tau/\text{tg}\gamma$ curves, derived from the tests at -110°C have been compiled in Fig. 34. Their grouping is such that the curves corresponding to $T_t = 310$ and 430°C constitute one group and those corresponding to $T_t = -110$ and $+191^\circ\text{C}$ another, while the curve for $T_t = 60^\circ\text{C}$ stands alone. This last-mentioned curve ascends very steeply up to the point of fracture. The curves consistent with untempered martensite and with $T_t = 191^\circ\text{C}$, respectively, have a fairly steeply rising initial portion, but this is followed by a distinct angulation and subsequent, virtually hori-

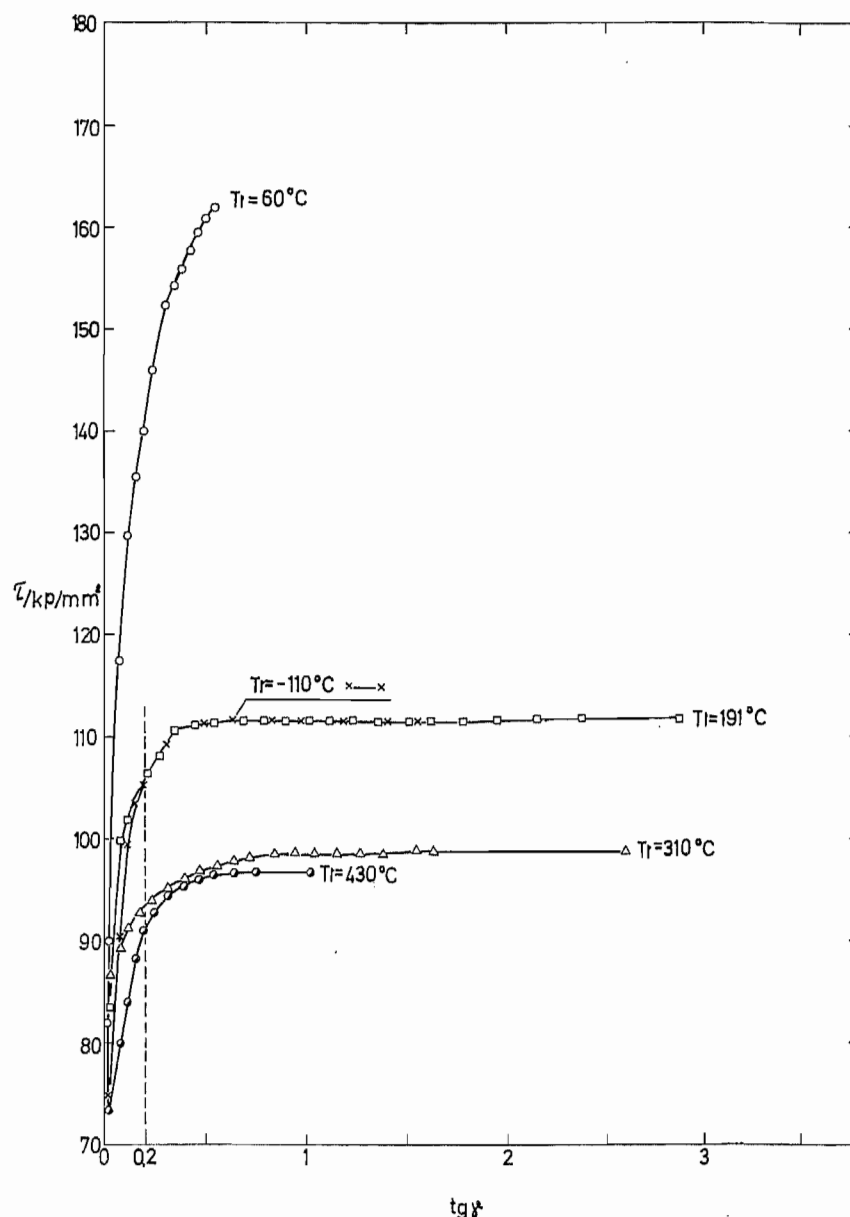


Fig. 34.

Shear stress - shear strain ($\tau/\text{tg}\gamma$) curves obtained at a testing temperature of $T_k = -110^\circ\text{C}$.
Speed of rotation $n = 0.074$ r.p.m.

zontal course for both curves. No angulation occurs in the curves corresponding to $T_t = 310$ and 430°C , and the work hardening continues up to high values of $\text{tg}\gamma$ in this case.

Tests at $+22^\circ\text{C}$. The $\tau/\text{tg}\gamma$ curves from the test series at room temperature are presented in Fig. 35. The curves corresponding to $T_t = 27$ and 430°C rise markedly and curve without angulation. Another rise appears in the curves corresponding to $T_t = 190$ and 310°C , consistent with the rise already discussed in connection with the series of tests at different speeds. This phenomenon was almost completely absent in the curves corresponding to the same tempering temperatures when the tests were carried out at -110°C .

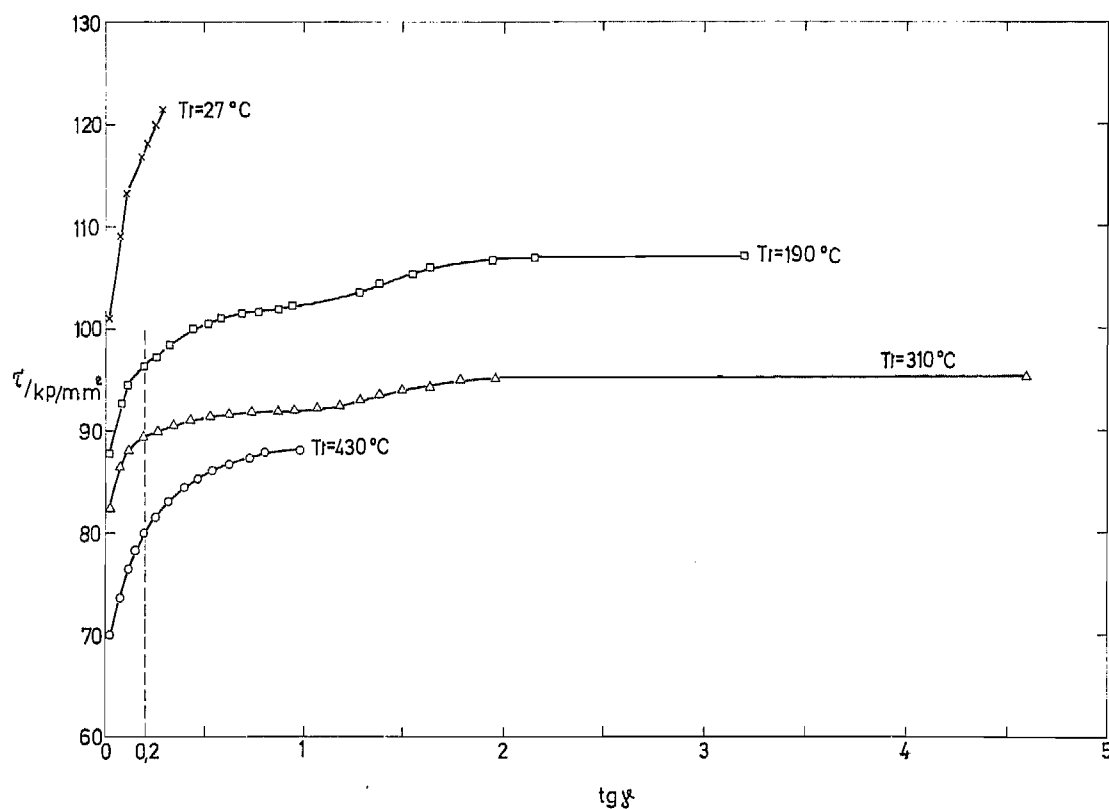


Fig. 35.
Shear stress-shear strain ($\tau/\text{tg}\gamma$) curves obtained at a testing temperature of $T_k = +25^\circ\text{C}$.
Speed of rotation $n = 0.074$ r.p.m.

Tests at $+95^\circ\text{C}$. The $\tau/\text{tg}\gamma$ curves obtained from the test series at $+95^\circ\text{C}$ are presented in Fig. 36. The curves obtained with specimens tempered at $T_t = 190$ and 310°C vary markedly and their ascent is more

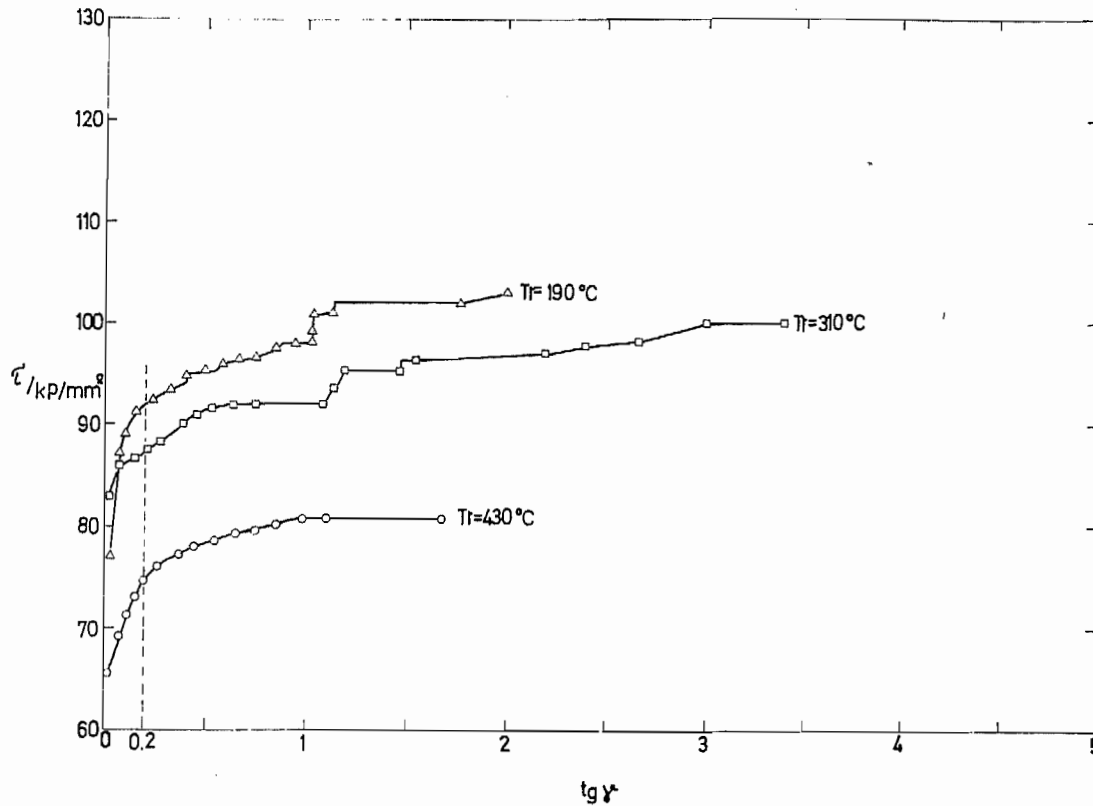


Fig. 36.

Shear stress-shear strain ($\tau/\text{tg}\gamma$) curves obtained at a testing temperature of $T_k = +95^\circ\text{C}$.
Speed of rotation $n = 0.074$ r.p.m.

noticeable than that of the corresponding $\tau/\text{tg}\gamma$ curves of tests at room temperature.

The observation is made on comparison of the $\tau/\text{tg}\gamma$ curves obtained in tests at different temperatures that increasing testing temperature causes them to shift downwards.

Local shear strain — length ($\text{tg}\gamma_l/l$) curves. Determination of the distribution of plastic deformation over the neck portion of the test bars twisted up to failure at different testing temperatures produced $\text{tg}\gamma_l/l$ curves similar to those previously discussed in connection with the test series involving different speeds of rotation (Fig. 31). These results referring to different testing temperatures and to structures achieved by different tempering treatments are presented in Fig. 37.

Examination of the effects exerted by the testing temperature on the distribution of deformation immediately reveals a comparatively negligible influence, as compared to that of the tempering temperature. The effect of the tempering temperature is manifest with particular clarity in the distribution

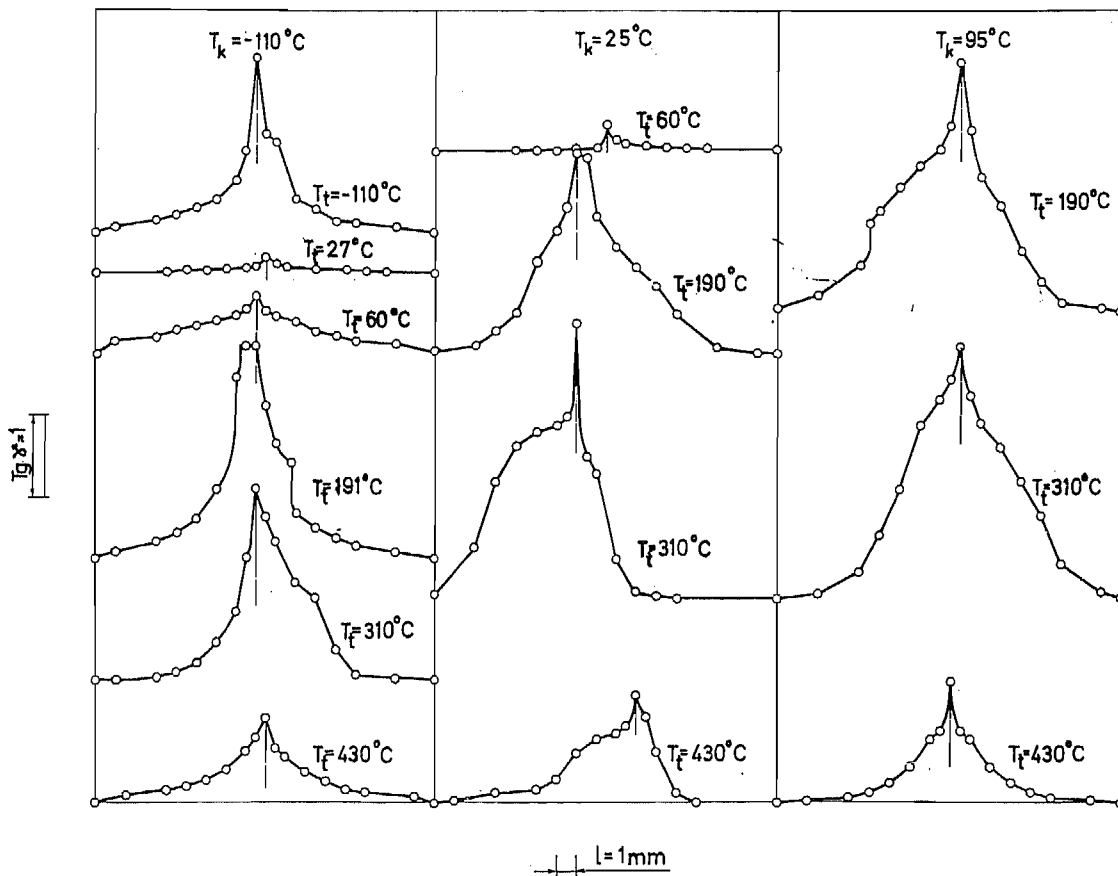


Fig. 37.

Local shear strain - length ($\text{tg}\gamma_1/l$) curves consistent with various tempering temperatures (T_t) and testing temperatures (T_k). Speed of rotation $n = 0.074$ r.p.m.

of plastic deformation displayed by the test bars twisted at -110°C . The distribution graph of untempered martensite ($T_t = -110^\circ\text{C}$) and of the test bars tempered at $T_t = 191, 310$ and 430°C has a high ridge, and the plastic deformation is mainly concentrated around the fracture. In the case of the test bar tempered at $T_t = 60^\circ\text{C}$, again, the curve is rather flat and the distribution of deformation over the neck portion more uniform than in the above-mentioned specimens. The test bar with $T_t = 27^\circ\text{C}$ suffered fracture after a very small amount of plastic deformation had occurred and the type of failure was rupture resulting from the tensile stress [41], whereas fracture by shearing occurred in the test bars which had been tempered at other temperatures [41]. If the $\text{tg}\gamma_1/l$ curves obtained from the tests carried out at different temperatures are compared, the curves corresponding to any given tempering temperature are found to be very similar. The curve consistent with $T_t = 60^\circ\text{C}$ is an exception: the test at room temperature with the test bar tempered at $+60^\circ\text{C}$ yields a $\text{tg}\gamma_1/l$ curve similar to that obtained in the test at -110°C with the test bar tempered at $+27^\circ\text{C}$.

3.2.3 Influence of tempering temperature on the results of the torsion test and notched-bar impact test

In order to obtain an overall idea of the manner in which the tempering temperature affects the toughness of hardened steel, test bars tempered at various temperatures were subjected both to torsion tests and to notched-bar impact tests, these tests being carried out at room temperature. In the torsion tests two speeds of rotation were employed: $n = 0.067$ and 640 r.p.m., and the notched-bar tests were made by the aid of a Charpy pendulum tester.

Torsion tests. The results obtained at low speed, $n = 0.067$ r.p.m., are presented in Fig. 38, in which the following quantities have been plotted over the tempering temperature: fracturing total twist (φ_{fr}), energy consumed in fracturing the bar (W), the maximum shear stress (τ_{max}) derived from the τ/φ curves, and the hardness (H_v).

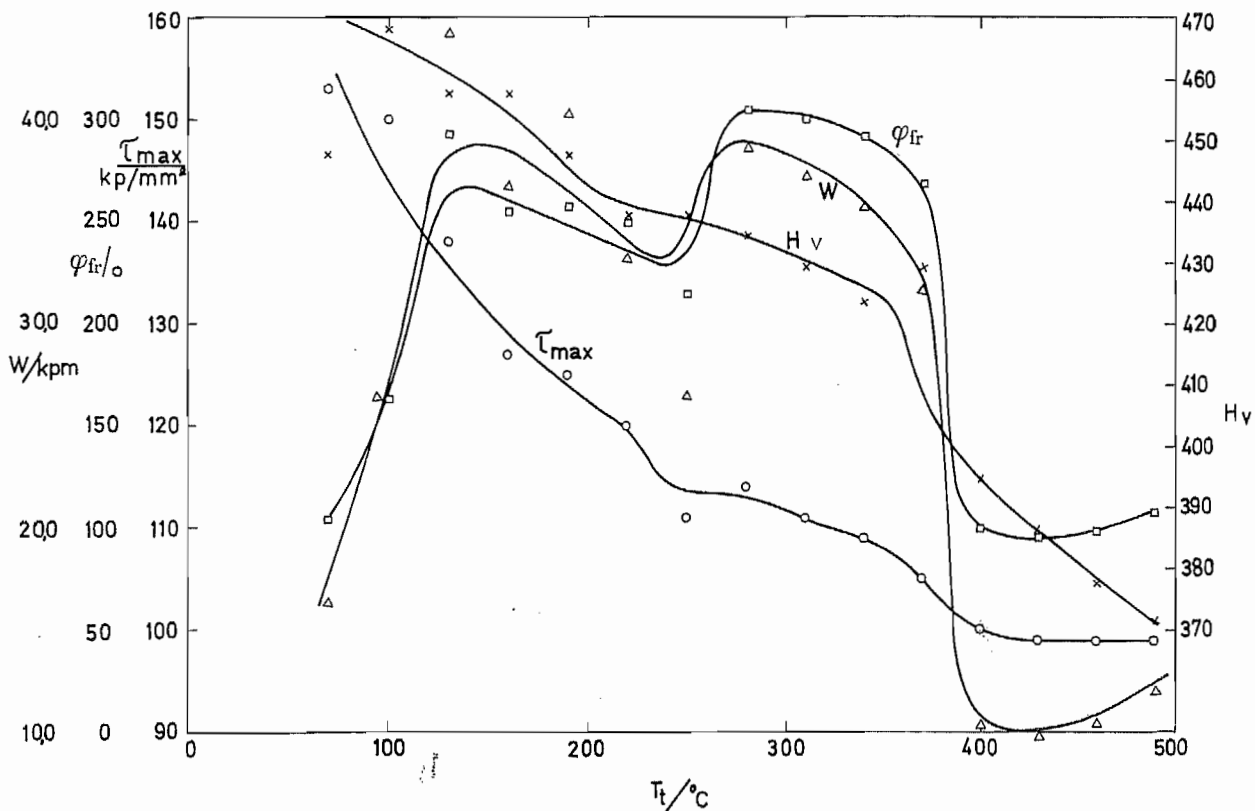


Fig. 38.

Fracturing total twist (φ_{fr}), energy consumed in fracturing (W), maximum shear stress (τ_{max}) found from the τ/φ curves and hardness (H_v) for test specimens tempered at various temperatures, as functions of tempering temperature (T_t). Speed of rotation $n = 0.067$ r.p.m., testing temperature $T_k = 25^{\circ}\text{C}$.

The fracturing total twist graph and that of the fracturing energy both increase at first with T_t . The neighbourhood of the tempering temperature $T_t = 180^\circ\text{C}$ is the region of a maximum; a slight minimum occurs around $T_t = 240^\circ\text{C}$, and another maximum is encountered about $T_t = 300^\circ\text{C}$. The curves finally turn into abrupt descent slightly below $T_t = 400^\circ\text{C}$.

The curves representing the maximum stress (τ_{\max}) and the hardness (H_v) decline fairly uniformly with increasing tempering temperature. However, a slight hump can be seen in the range of $T_t = 250 - 360^\circ\text{C}$.

The results derived from the torsion tests at high speed, $n = 640$ r.p.m., are presented in Fig. 39, which contains the same quantities as Fig. 38 except for the hardness, viz., φ_{fr} , W and τ_{\max} . All three curves have a maximum at about $T_t = 70^\circ\text{C}$. At tempering temperatures above this maximum range, the curve representing the stress declines uniformly, while the fracturing total twist and fracturing energy curves have a minimum in the interval $T_t = 190 - 330^\circ\text{C}$.

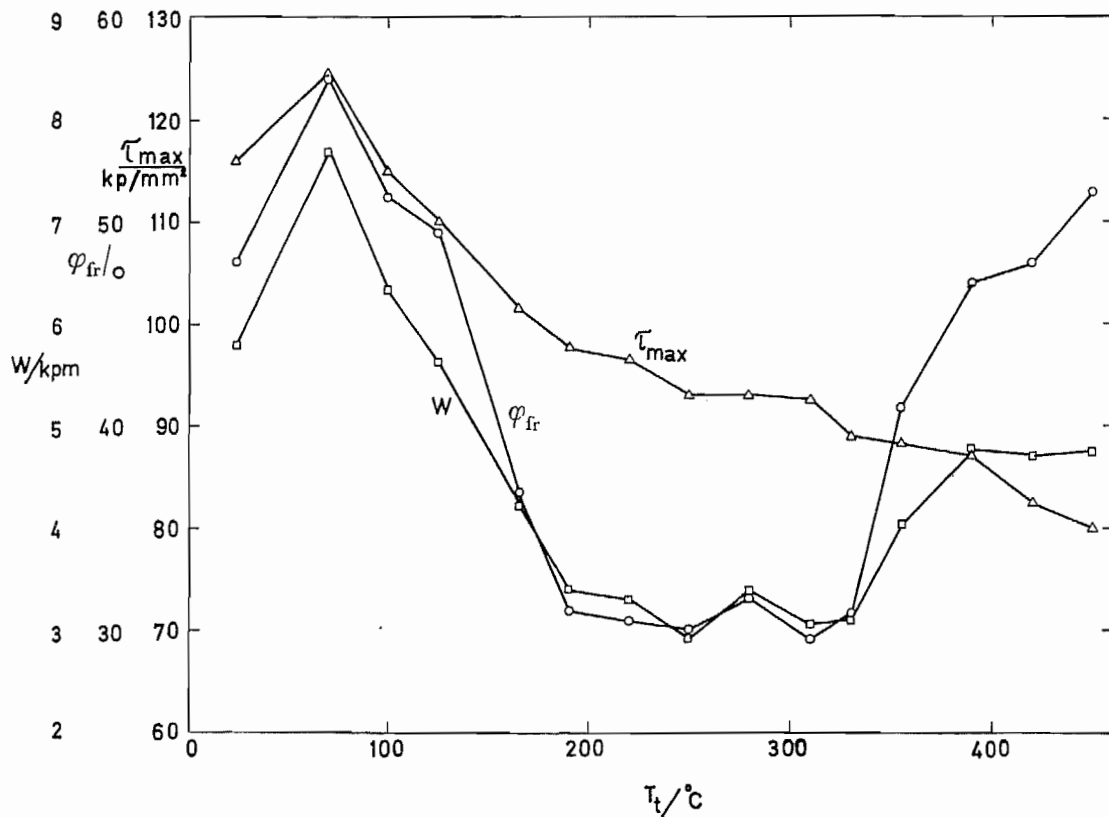


Fig. 39.

Total twist (φ_{fr}), energy consumed in fracturing (W) and maximum shear stress (τ_{\max}) found from the τ/φ curves for test specimens tempered at various temperatures, as functions of the tempering temperature (T_t). Speed of rotation $n = 640$ r.p.m., testing temperature $T_k = +25^\circ\text{C}$.

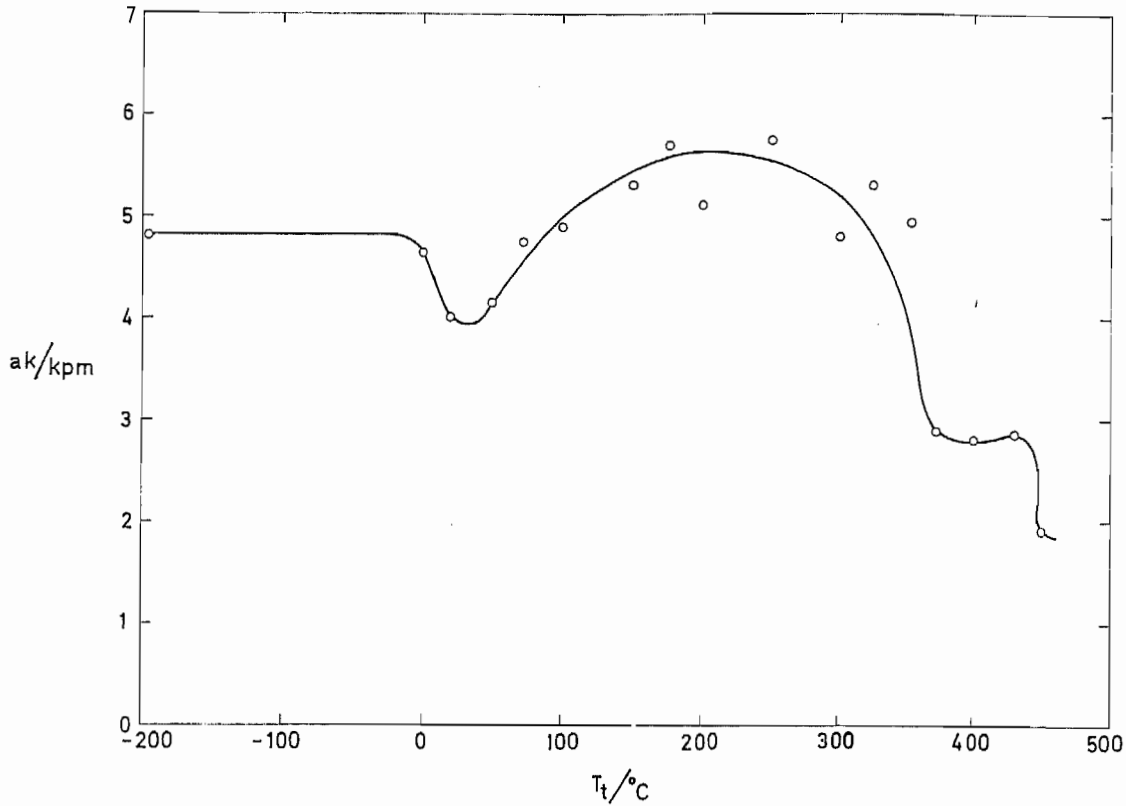


Fig. 40.

Notched-bar impact toughness (ak) values found for test bars tempered at various temperatures. Testing temperature $T_k = +25^{\circ}\text{C}$.

If the φ_{fr}/T_t and W/T_t curves in Figs. 38 and 39 are considered, the observation can be made that they run at much lower levels in Fig. 39 than in Fig. 38. It is also to be noted that the curves have minima in Fig. 39 at the same temperature intervals at which maxima were observed in Fig. 38.

Notched-bar impact tests. The materials to be tested could be expected to present a fairly high degree of brittleness, and test bars having only a shallow notch (Fig. 15) were therefore used in the notched-bar tests. The values of the impact toughness (ak) found for the test bars tempered at different temperatures are presented in Fig. 40.

It is seen from Fig. 40 that the ak curve has a minimum in the range of about $T_t = 20^{\circ}\text{C}$ and a maximum around $T_t = 200^{\circ}\text{C}$. The curve declines at temperatures higher than the last-mentioned value.

The course of the ak/T_t curve derived from the notched-bar impact tests in Fig. 40 closely resembles that of the graph obtained for the fracturing energy, W/T_t , from the series of torsion tests at low speed, Fig. 38.

3.3 Deformed structure

In order to clarify the effects exerted by deformation on the structure of the tempered steel, electron microscopy of the deformed test specimens was undertaken, employing the surface replica and thin foil methods. The specimens were test bars tempered at $T_t = 70, 190$ and 310°C , which had been tested in the torsion machine at low speed, $n = 0.0677$ r.p.m.

Figs. 41 and 42 show the deformation marking on the polished surface of a specimen tempered at $T_t = 70^\circ\text{C}$. Slip lines belonging to two systems can be observed, which cross each other. The slip bands are fairly straight, but they are somewhat forked in appearance.

In Figs. 43 and 44, traces of deformation on the surface of a specimen tempered at $T_t = 190^\circ\text{C}$ are presented. Thick slip lines running in a certain principal direction can be seen. They are interrupted by the martensite lenses, and slip in the principal direction does not seem acceptable in the lenses (Fig. 44). The slip occurring in such lenses has taken place in a direction differing from the principal direction, with highly complex slip bands.

Figs. 45 and 46 show traces of deformation on the surface of a specimen tempered at $T_t = 310^\circ\text{C}$. Slip bands consistent with at least two intersecting systems are observable, resulting in a terraced appearance of the surface.

Micrographs of surface replicas taken from deformed, polished and etched specimens are presented in Figs. 47, 48 and 49, corresponding to a tempering temperature of $T_t = 310^\circ\text{C}$. Fig. 47 shows an area which has undergone only little deformation. It reveals deformation bands (A) passing over numerous lenses, and many areas of retained austenite. In the band, the carbide plates have assumed an orientation deviating from the normal system. Fig. 48 represents an area with comparatively high deformation. Here, too, regional rotations of the carbide system (A) can be observed. Deformed carbide plates are encountered on the boundaries of such areas with changed orientation.

Fig. 49 is a micrograph from a strongly deformed area. Almost all carbide plates have now assumed the same orientation; elongation of the structural elements is a characteristic feature.

Figs. 50 and 51 show thin foil pictures of samples from a deformed test bar, corresponding to a tempering temperature of $T_t = 310^\circ\text{C}$. Fig. 50 shows an area where the deformation has been slight, and slightly bent carbide plates are visible (cf. Fig. 21). In Fig. 51, which represents an area of strong deformation, deformed carbides (A) and bands (B) can be seen, which were already observed in the surface replica, Fig. 48.

Replica and thin foil electron micrographs were also made of test bars fractured at high speed, $n = 42.1$ r.p.m., in the torsion testing machine. The observations made from them contain nothing that would be at variance with that reported in the foregoing.

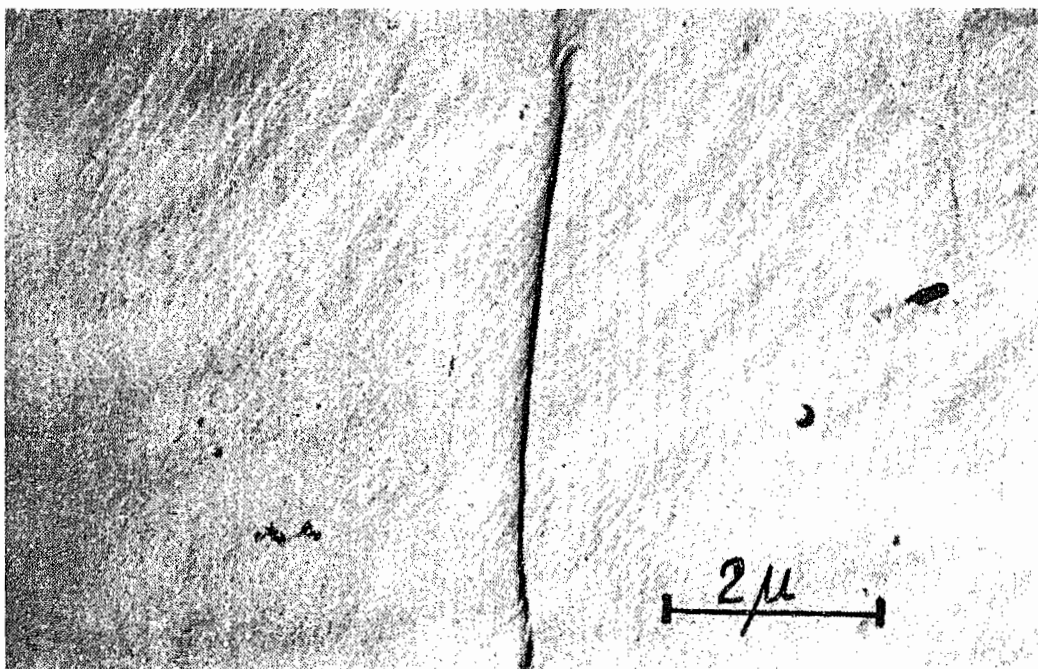
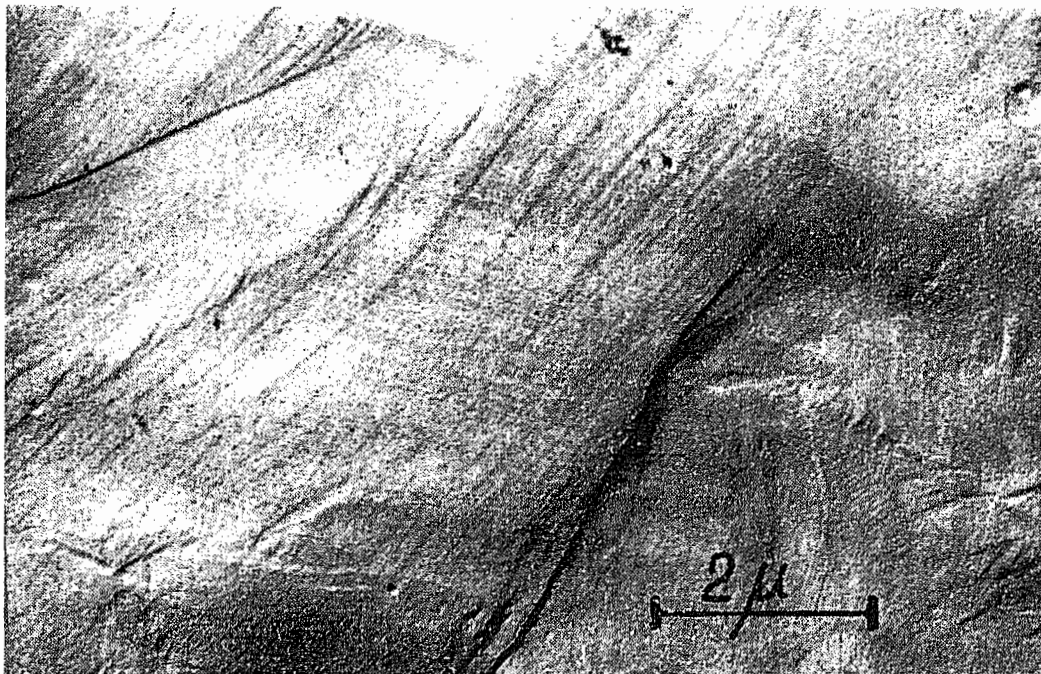


Fig. 41 and 42.
Deformation markings on the surface of a test specimen tempered at $T_t = 70^\circ\text{C}$.

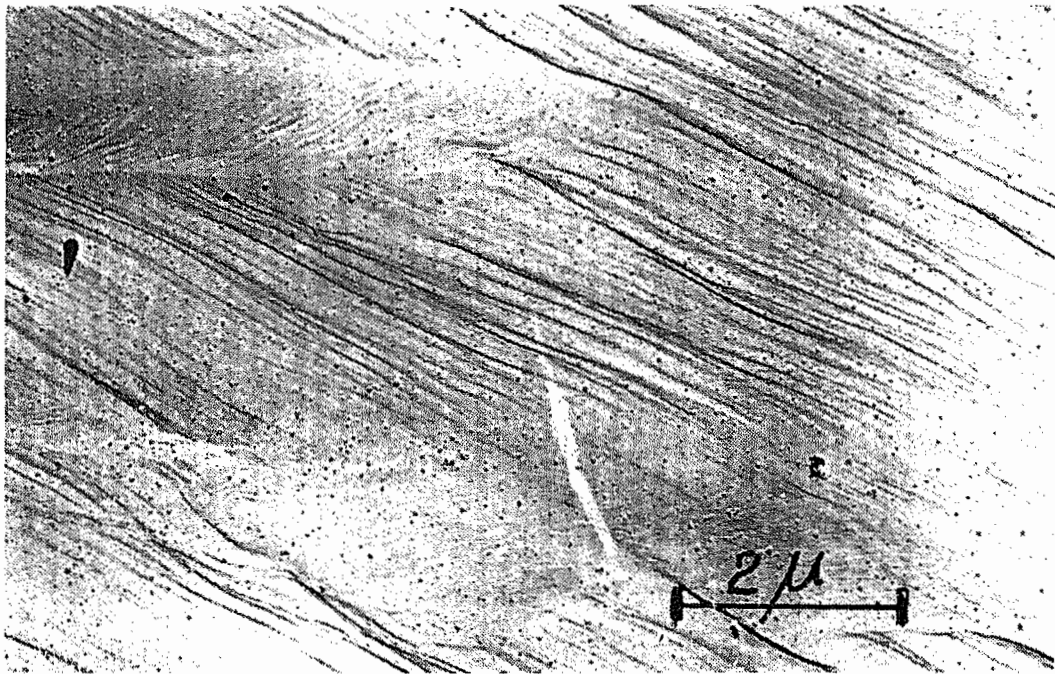
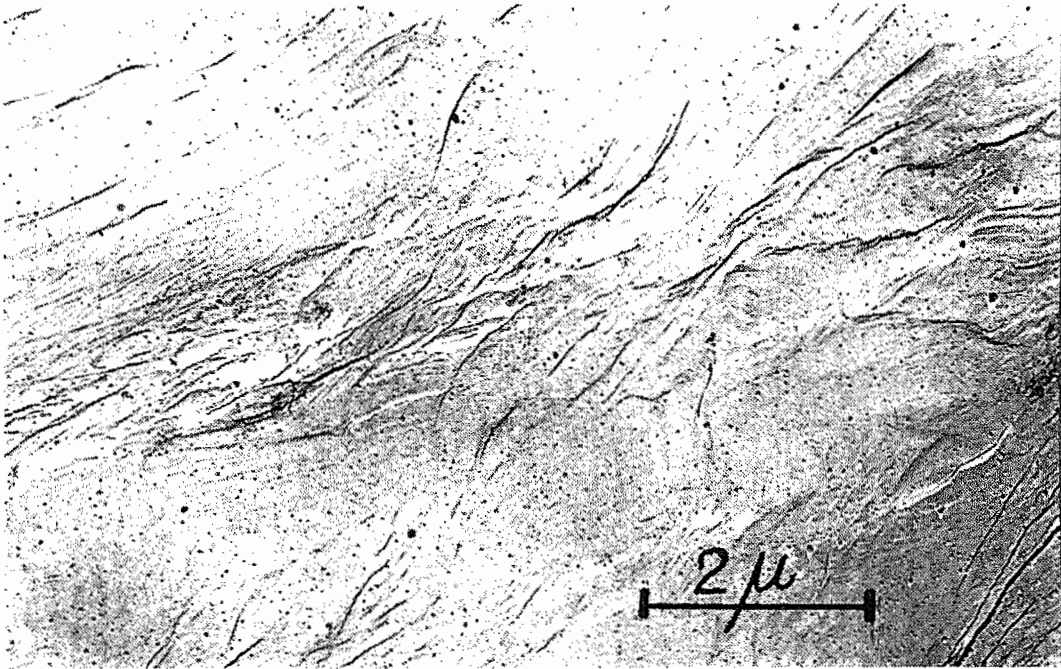


Fig. 43 and 44.

Deformation markings on the surface of a test specimen tempered at $T_t = 190^\circ\text{C}$.

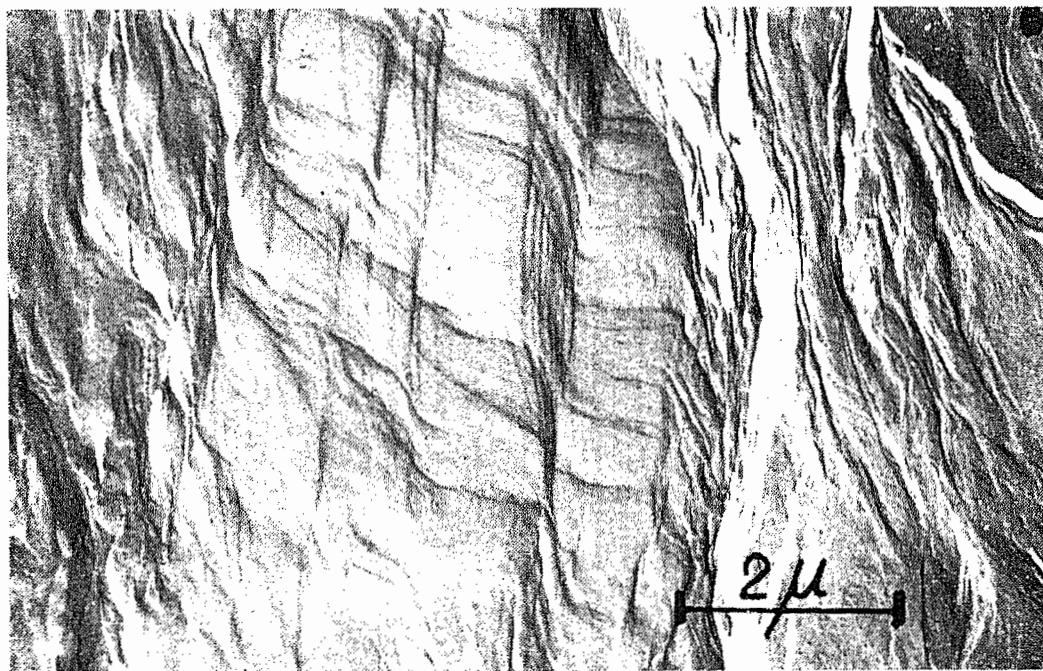


Fig. 45 and 46.
Deformation markings on the surface of a test specimen tempered at $T_t = 310^\circ\text{C}$.

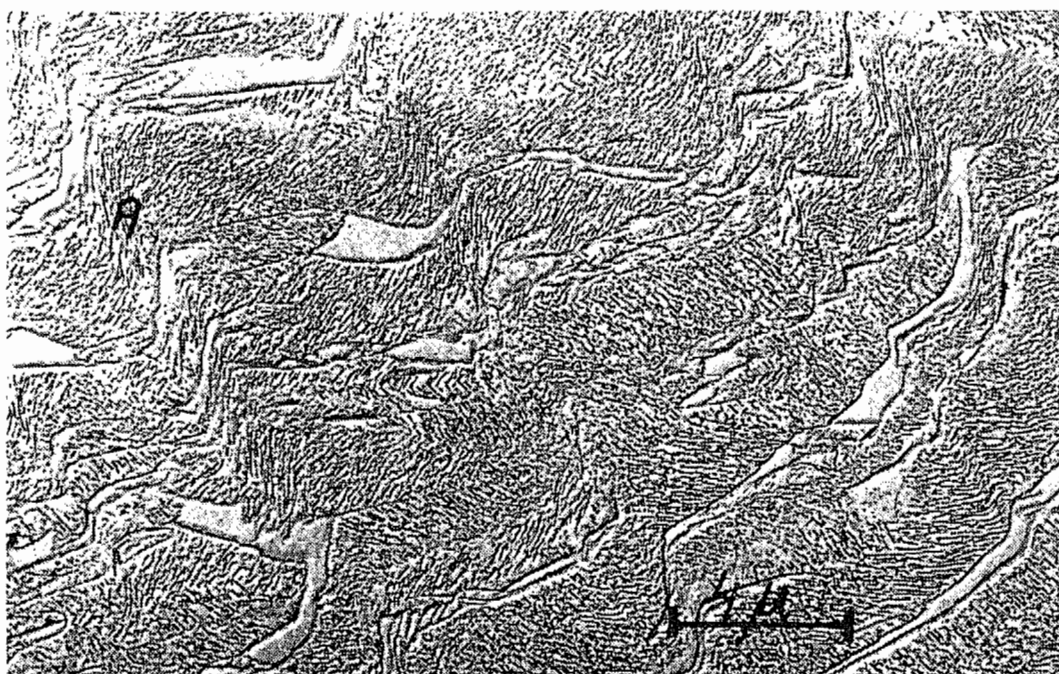


Fig. 47.
Deformation bands (A) in a slightly deformed test specimen. Tempering temperature $T_t = 310^\circ\text{C}$. (Replica of polished specimen.)



Fig. 48.
Deformation bands (A) and deformed carbide plates in a deformed test specimen. Tempering temperature $T_t = 310^\circ\text{C}$. (Replica of polished specimen.)



Fig. 49.

Carbide plates in parallel orientation in a strongly deformed test specimen. Tempering temperature $T_t = 310^\circ\text{C}$. (Replica of polished specimen.)

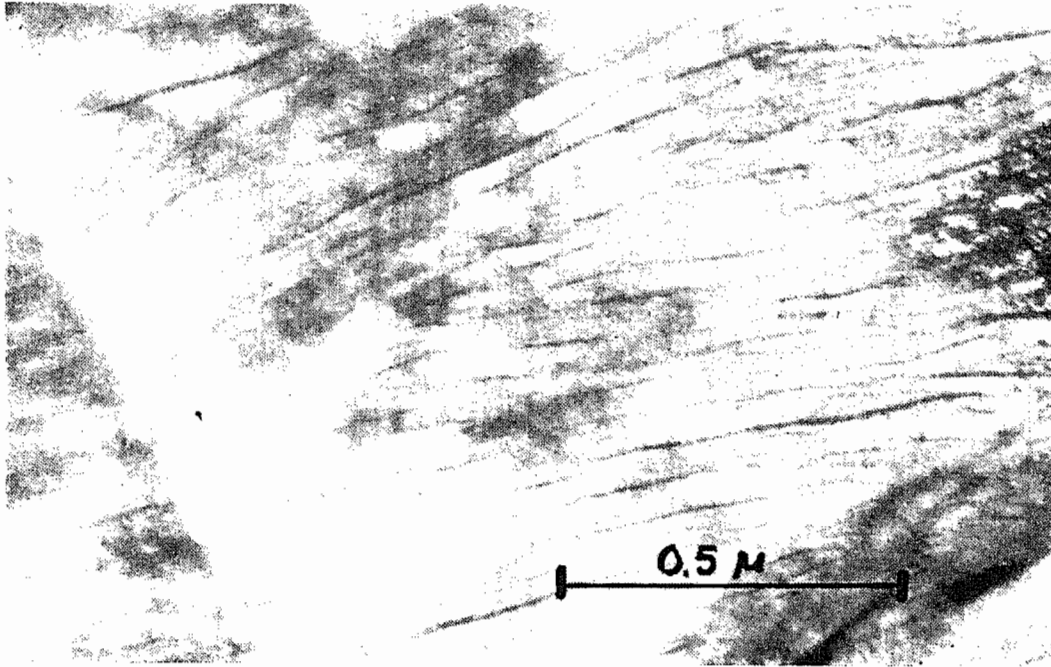


Fig. 50.
Slightly bent carbide plates. Tempering temperature $T_t = 310^\circ\text{C}$ (Thin foil electron micrograph.)



Fig. 51.
Strongly deformed carbide plates (A), and deformation band (B). Tempering temperature $T_t = 310^\circ\text{C}$. (Thin foil electron micrograph.)

4. DISCUSSION

The experimental results reported in the preceding chapter will now be discussed with regard to the elucidation of the following aspects: work hardening, effects of the testing temperature, effects of the speed of rotation, and effect of the tempering temperature on the toughness of hardened steel.

4.1 Work hardening

When hardened steel is tempered, precipitation reactions take place in the martensite, as a result of which different carbides are produced according to the composition of the steel. The following general idea of the effects exerted by such precipitation has been formulated in numerous investigations [42]. When coherent precipitates are produced, the yield strength increases substantially, while the rate of work hardening remains comparatively low, at the level it also has in solid solutions. Fracture only occurs after plastic deformation of remarkable magnitude. The slip lines remain weakly pronounced [43]. Dislocations cut precipitates. When the precipitates become incoherent and grow, the yield strength is clearly lowered but the rate of work hardening increases. Fracture will now ensue upon fairly small plastic deformation [42]. The rate of work hardening frequently decreases with increasing testing temperature [44].

Consideration of the τ/ϕ curves (Fig. 33) and $\tau/\text{tg}\gamma$ curves (Figs. 34 and 35) obtained for the steel used in this work after various tempering treatments reveals that tempering has had a marked influence not only on the yield strength but also on the rate of work hardening and on the value of $\text{tg}\gamma$ at which fracture occurred. In the case of untempered martensite ($T_t = -110^\circ\text{C}$), the $\tau/\text{tg}\gamma$ curve initially rises steeply, but a distinct knee is seen at $\text{tg}\gamma = 0.4$, after which the course of the curve is virtually horizontal. In contrast with this, the curve corresponding to the tempering temperature $T_t = 60^\circ\text{C}$ ascends very steeply up to the point of fracture. After tempering at $T_t = 191^\circ\text{C}$, the $\tau/\text{tg}\gamma$ curve is largely similar to that of untempered martensite, but the $\text{tg}\gamma$ value consistent with the point of fracture is considerably higher. The $\tau/\text{tg}\gamma$ curves corresponding to $T = 310$ and 430°C have no points of angula-

tion. In the case of the latter, however, the rate of work hardening is considerably higher.

Perhaps the most remarkable change encountered in the $\tau/\text{tg}\gamma$ curves is the powerful rate of work hardening associated with ageing of martensite (Fig. 34, $T_t = 60^\circ\text{C}$). It is obvious that the strong changes in rate of work hardening are not directly caused by the interstitial atoms in solution, carbon and nitrogen. Quite evidently they must be caused by grouping of these atoms, of which our understanding is still very incomplete. It is not known by what kinds of atom groups they are caused, because no precipitates have been observed in thin foil electron micrographs [22]. There is no doubt that interstitial atoms must have come out of solution, since the dilatometric measurements reveal that considerable decrease of the relative length takes place (Fig. 16).

It might be suggested as an explanation for the high rate of work hardening of aged martensite that the onset of parabolic hardening would be inhibited in the structure in question and the deformation would occur in the linear hardening stage to a high degree. During the parabolic stage, screw dislocations by-pass obstacles by cross slip and are possibly annihilated when they encounter screw dislocations of opposite sign. One of the necessary prerequisites for cross slip is that the dislocations have straight portions of a length sufficient to result in starting resistance to cross slip of low order. If a dislocation is highly bowed by reason of its avoidance of the precipitates, cross slip cannot take place. This would seem to be the case with $T_t = 60^\circ\text{C}$ (Fig. 34). The slip lines produced on the surface of the test specimen are then thin and fairly straight and such lines occur in at least two intersecting systems (Figs. 41 and 42). This seems to suggest the linear stage, at which the rate of work hardening is high.

Another explanation to account for the inhibition of cross slip would be that the dislocations are extended and the constriction necessary for cross slip to be possible does not occur at the low temperatures concerned here.

The corresponding data referring to the tempering temperature $T_t = 191^\circ\text{C}$ tends to support the explanation involving cross slip. The rate of work hardening of the specimens with this tempering treatment is less and becomes almost zero when the shear strain is $\text{tg}\gamma = 0.4$. The slip lines seen on the test specimens are fairly thick in this case. Such thickening of the slip lines has previously only been associated with parabolic hardening [45].

The $\tau/\text{tg}\gamma$ curve consistent with $T_t = 310^\circ\text{C}$ (Figs. 34 and 35) is close to what is usually considered characteristic of a structure containing coherent precipitates: the rate of work hardening is low, and the deformation continues far [42]. Coherent or semi-coherent precipitates are also evident from Figs. 47, 48, 49, 50 and 51: they all show deformed carbide plates, the lattice structure of which could not be clarified in this work, as already stated. They are very small, about 20 \AA in thickness and about $1\,000\text{ \AA}$ in length. Since it is hard

to imagine that such small precipitates can contain their own dislocation system independent of the matrix, there is no possibility other than that the dislocations moving in the matrix cut the precipitates. When this occurs, cross slip is unnecessary.

The $\tau/\text{tg}\gamma$ curve corresponding to $T_t = 430^\circ\text{C}$ has no point of angulation (Figs. 34 and 35). The rate of work hardening is high, and fracture occurs at small values of $\text{tg}\gamma$. The diagram resembles the type commonly associated with a structure containing incoherent precipitates or precipitates otherwise difficult to be cut by a dislocation, and in which the slipping becomes turbulent. It can be seen from Figs. 24 and 25 that the precipitates are already very large. Moreover, they could be positively established as cementite (Section 3.1.2), which has a complicated lattice structure creating a condition in which dislocations only cut precipitates with difficulty.

4.2 Effects of testing temperature

4.2.1 Level of the $\tau/\text{tg}\gamma$ curves

It is observable from Figs. 34, 35 and 36 that the $\tau/\text{tg}\gamma$ curves shift downwards when the testing temperature increases from -110°C through $+25^\circ\text{C}$ to $+95^\circ\text{C}$.

For numerical assessment of the effect exerted by the testing temperature on the yield stress, as regards the value it attains in the course of deformation, we consider the yield stress $\tau_{\text{tg}\gamma=0.2}$ corresponding to a shear strain equal to $\text{tg}\gamma = 0.2$. At higher values of $\text{tg}\gamma$, anomalies are seen in the $\tau/\text{tg}\gamma$ curves obtained at higher testing temperatures, which may be due to changes in structure occurring during the test; it is therefore doubtful whether the corresponding yield stresses are consistent with the original structure.

When the $\tau_{\text{tg}\gamma=0.2}$ values of the yield stress found from the $\tau/\text{tg}\gamma$ curves for different testing temperatures are plotted over the temperature in the test, the graphs presented in Fig. 52 are obtained for the various tempering temperatures. They are quite nearly straight lines ascending at the rate of 6.8 kp/mm^2 per 100°C ($T_t = 190^\circ\text{C}$), 3.0 kp/mm^2 per 100°C ($T_t = 310^\circ\text{C}$) and 7.8 kp/mm^2 per 100°C ($T_t = 430^\circ\text{C}$), respectively. It is to be noted that the dependence of $\tau_{\text{tg}\gamma=0.2}$ on temperature is least in the instance of the tempering temperature $T_t = 310^\circ\text{C}$. This implies that the significance of thermal activation is less in the deformation of the test specimens tempered at $T_t = 310^\circ\text{C}$ than in that of specimens with other tempering temperatures. The deformation mechanism in the test specimens tempered at 310°C must therefore be different from that operating in the specimens which were tempered at 190 and 430°C .

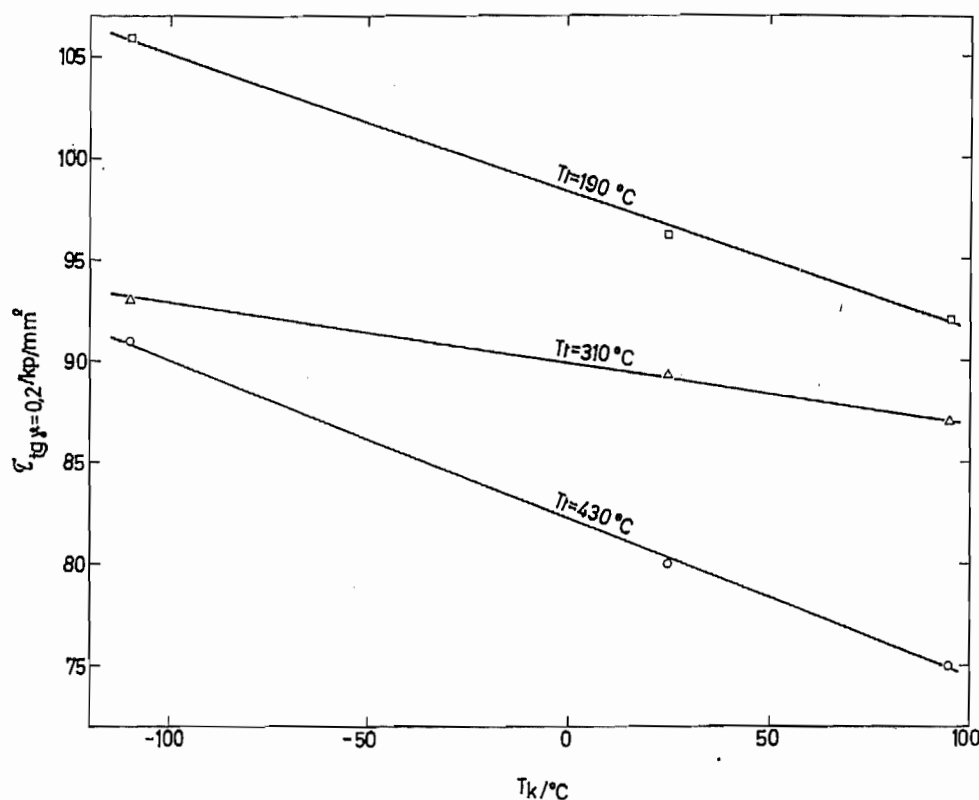


Fig. 52.

Values of the yield stress $\tau_{tg\gamma=0.2}$ corresponding to a shear strain of $tg\gamma = 0.2$, obtained at various testing temperatures (T_k) for different tempering temperatures (T_t).

Complete clarity could not be obtained in the present work of the cause of the difference in temperature dependence of $\tau_{tg\gamma=0.2}$. In the preceding paragraph, however, the possibility was pointed out that the motion of dislocations might be turbulent in the specimens tempered at $T_t = 430^\circ\text{C}$. Likewise, occurrence of cross slip in the case with specimens tempered at $T_t = 190^\circ\text{C}$ was assumed, while no such assumption was necessary when the tempering had been carried out at $T_t = 310^\circ\text{C}$.

Accordingly, the need of thermal activation would only have been marked in cases where $T_t = 190$ and 430°C .

4.2.2 Shape of the $\tau/tg\gamma$ curves

Comparisons between Figs. 34, 35 and 36 show that the shape of the $\tau/tg\gamma$ curves varies according to testing temperature (T_k). When, in particular, the testing temperature was $T_k = +95^\circ\text{C}$, the first rise of the curves is followed by another rise or indeed by several, which are absent at the testing temperature $T_k = -110^\circ\text{C}$. Since these ascending portions only appear in

curves obtained at high temperatures, they are obviously caused by phenomena requiring thermal activation. An ageing phenomenon similar to that of blue brittleness may be concerned, which manifests itself in a stepwise rise of the stress-strain curves obtained in tension tests [40].

4.3 Effects of speed of rotation

Earlier studies of the effects exerted by the rate of deformation have shown that the resistance to deformation increases with increasing rate of deformation in most tough metals. It has however been noted that frequently the capacity of deformation increases with the rate of deformation [46].

The τ/φ and $\tau/tg\gamma$ curves obtained in the present work from tests with tempered martensite are observed to shift downward when the speed of rotation in the torsion test is increased (cf. e.g. Fig. 28). Thus in the case of tempered martensite the effect of testing speed was opposite to that reported for other cases. Furthermore, other particular effects were elicited with tempered martensite when the testing speed was varied. They will be discussed in greater detail in the following.

4.3.1 Heating of the test bar

As previously noted (page 49), the test bar was found to experience considerable heating at high testing speeds.

If it is assumed that all the work expended on each volume element of the test bar is transformed into heat and that this heat is not dissipated by conduction, the rise in temperature of the volume element, ΔT , at increase of its deformation to $tg\gamma$ is found to be:

$$\Delta T = \frac{\int_0^{tg\gamma} \tau(tg\gamma) d tg\gamma}{\varrho \cdot C} \quad (3)$$

where $\tau(tg\gamma)$ = the acting shear stress,

ϱ = density,

C = specific heat.

Equation (3) states the absolute upper limit of the increase in temperature (ΔT) of the element.

It is seen from Fig. 29 that at the speed $n = 160$ r.p.m. the τ values corresponding to $T_t = 190$ and 310°C vary only little with $\text{tg}\gamma$. The average stress may therefore be taken as $\tau = 90$ kp/mm² for $T_t = 190^\circ\text{C}$, and $\tau = 87$ kp/mm² for $T_t = 310^\circ\text{C}$. For a density $\rho = 7.8 \cdot 10^{-6}$ kg/mm³ and a specific heat, $C = 0.11$ kcal/kg $\cdot^\circ\text{C}$, we find:

$$\begin{aligned}\Delta T/^\circ\text{C} &= 246 \cdot \text{tg}\gamma & (T_t = 190^\circ\text{C}) \\ \Delta T/^\circ\text{C} &= 238 \cdot \text{tg}\gamma & (T_t = 310^\circ\text{C})\end{aligned}\quad (4)$$

At the values of $\text{tg}\gamma$ measured in the present work, the temperature may rise several hundred degrees, provided that by reason of the rapid deformation the heat does not have time to be transferred away from the area undergoing deformation.

On the other hand, the increase in temperature associated with deformation can be estimated on the basis of the temperature dependence of $\tau_{\text{tg}\gamma = 0.2}$, starting from the assumption that the results presented in Fig. 52 are also valid at high speeds of rotation and with all values of $\text{tg}\gamma$. As an example, let us consider the case consistent with $T_t = 190^\circ\text{C}$. We find for $\tau_{\text{tg}\gamma = 0.2}$ at room temperature and at low speed, $n = 0.074$ r.p.m., from Fig. 35 the value 96.2 kp/mm², and at high speed, $n = 42.1$ r.p.m., from Fig. 29 the value 94.6 kp/mm². Consistent with the difference in stress, (96.2 – 94.6) kp/mm² = 1.6 kp/mm², Fig. 52 shows that the increase in speed of rotation from 0.074 to 42.1 r.p.m. corresponds to a temperature difference of $\Delta T = 24^\circ\text{C}$. Assuming that the temperature remains unchanged, at 25°C , when the speed is low ($n = 0.074$ r.p.m.), the temperature of the area undergoing the strongest deformation will thus rise to 49°C when the speed increases from $n = 0.074$ r.p.m. to $n = 42.1$ r.p.m. When the same consideration is applied to other values of $\text{tg}\gamma$, the curve marked 1A in Fig. 53 is obtained for the temperature rise occurring at a speed of $n = 42.1$ r.p.m. Similarly, curve 2A is found for the speed of $n = 160$ r.p.m., while curves 1B and 2B result when the calculation is made for $T_t = 310^\circ\text{C}$ and for $n = 42.6$ and 160 r.p.m., respectively.

It is thus understandable that the curves 1A, 1B, 2A and 2B indicate the temperatures attained by the points in the test bar subject to strongest deformation when the tests are performed at room temperature. On the basis of Fig. 53, they can be compared to the curves illustrating the relationship of ΔT and $\text{tg}\gamma$ according to equations (4) (Curves 1 and 2), which have also been entered in the figure, and which were previously deduced on the assumption that no heat escapes from the area undergoing deformation while the test is in progress.

The curves 1A, 1B, 2A and 2B are all positioned close to curves 1 and 2 or somewhat below; the latter indicates that heat is dissipated during the test from the points undergoing deformation. However, this transfer of heat becomes

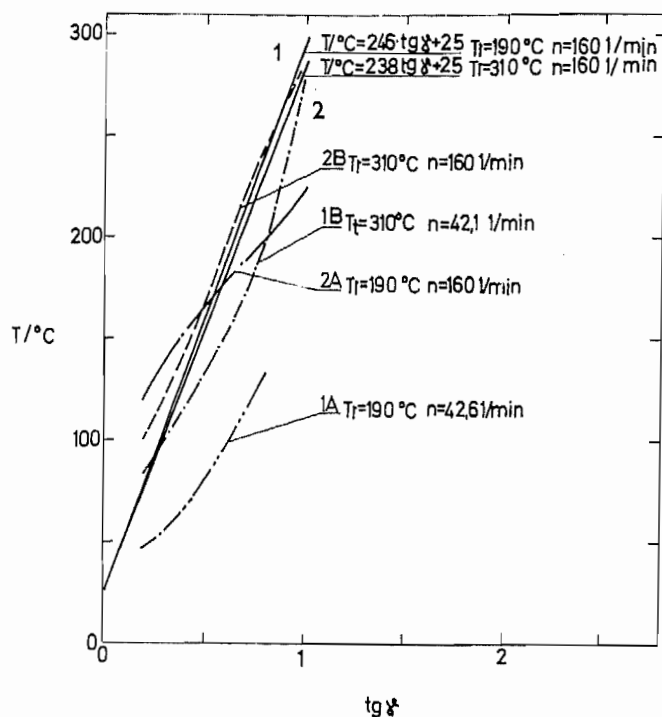


Fig. 53.

Temperature (T) of the test bar, calculated on the assumption that no heat is dissipated from the deformed region during the test, curves No. 1 and 2. (Consistent with speed of rotation $n = 160$ r.p.m.). – Curves 1A and 1B, 2A and 2B are consistent with the assumption that the lowering of yield stress observable with increasing speed of rotation would be exclusively due to temperature rise.

less as the speed of rotation is higher, seeing that the curves 2A and 2B run above curves 1A and 1B. It should also be noted that the values of $\text{tg } \gamma$ constituting the basis for the curves discussed here are consistent with the macroscopic observations, whereas the deformation is actually concentrated on exceedingly small areas. The local increase in temperature may therefore come very close to that predicted by the theoretical curves 1 and 2.

It has been noted earlier that the $\tau/\text{tg } \gamma$ curves (Fig. 29) turn into decline at high speed when $\text{tg } \gamma$ passes a given, critical value. This is probably caused by the fact that the bars are heated up at high speeds of rotation, their increase in temperature increasing with $\text{tg } \gamma$, as has been shown. With increasing temperature, the yield stress is reduced (cf. Fig. 52), and when this reduction is large enough, it is able to compensate for the effect of work hardening. When a given value of $\text{tg } \gamma$ has been exceeded, it even outweighs the work hardening and the curve will assume a falling trend. It should also be taken into account that the rate of work hardening is known to decrease with increasing temperature [47]; the course of the $\tau/\text{tg } \gamma$ curve will consequently assume the character shown in Fig. 54 by reason of the temperature rise.

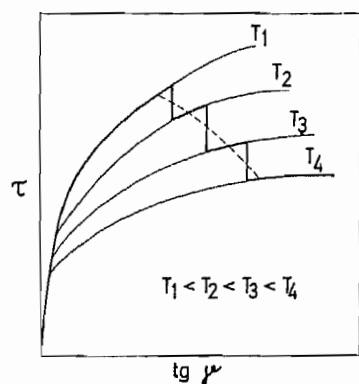


Fig. 54.

Schematic diagram showing the effect of temperature on yield stress (τ) and rate of work hardening. [47].

4.3.2 Concentration of deformation

The dependence of toughness on the speed of rotation in the torsion test is particularly clearly seen in Fig. 30. For instance, the fracturing total twist (φ_{fr}) of the test specimens tempered at $T_t = 310^\circ\text{C}$, which is high at small speeds, drops to very low values when the speed of rotation passes a certain critical value lying between $n = 4.26$ and 42.6 r.p.m. Fig. 31 reveals this decline to be primarily due to the fact that the plastic deformation, which spreads all over the neck portion of the test bar at low speeds, becomes concentrated to a narrow zone when the speed is high (e.g., $n = 320$ r.p.m.); the fracturing total twist then remains small even if the local values of $tg\gamma$ should be quite high (e.g. at $n = 42.1$ r.p.m.).

It is of decisive importance from the viewpoint of toughness that the deformation will not concentrate to a limited area, at least not at an early stage; the toughness is thus not determined by the capacity of deformation in itself, i.e., by high $tg\gamma$ values alone. The concentration of deformation is inhibited particularly when the rate of work hardening is high, although a very high rate of work hardening results in rapid increase of the yield stress, and thus in fracture at small deformation.

It was shown in the preceding paragraph that a rate of work hardening can be eliminated by softening caused by an increase in temperature. It was also shown that a local rise in temperature can occur with increasing $tg\gamma$ when the speed of rotation (n) is high enough to preclude equalization of temperature. This explains why, particularly in the case of $T_t = 310^\circ\text{C}$ (Fig. 31), the deformation is concentrated to a very narrow zone at high speeds, with the result that the fracturing total twist (φ_{fr}) remains small (Fig. 30).

On the basis of the results presented heretofore, the development of deformation can be described as follows: Under the influence of a shear stress, the bar is at first twisted in such a manner that the deformation will be uniformly

distributed over its neck portion. As soon as $tg\gamma$ increases at some point to such magnitude that the corresponding temperature rise (cf. Fig. 53) suffices to compensate for the rate of work hardening, the $\tau/tg\gamma$ curve will turn into decline (Fig. 29), when the condition will be unstable with regard to stress. When the resistance to deformation becomes less at the point in question, the energy stored in the form of elastic stress in various mechanical elements of the testing machine is discharged and carries the deformation in this area forward at a high rate. This results in formation of a narrow deformation band. Since the band is rapidly produced, the temperature in the region concerned will rise very rapidly, thus further decreasing the resistance against deformation. The amount of deformation produced at such a surge will primarily depend on the design of the testing machine.

The value of $tg\gamma$ at which concentration of deformation occurs depends on the speed of rotation. At high speeds, when the temperature rise becomes localized, its effects compensate for the rate of work hardening at small values of $tg\gamma$, which is evident from the $\tau/tg\gamma$ curves (Fig. 29), and concentration of deformation occurs at an earlier stage (Fig. 31) with about the same $tg\gamma$ values. However, such concentration will also take place at small speeds after $tg\gamma$ has become large enough for the $\tau/tg\gamma$ curve to assume a horizontal course (Figs. 28 and 31).

4.3.3 Pulsating deformation

In the τ/φ curves presented in Fig. 26, two waves were observed to occur, and the ascending parts of the latter wave were marked A – B. In the $\tau/tg\gamma$ curves (Fig. 29), they call forth a vertical rise, A – B. During this phase the deformation was observed to spread so that a broad band was formed on the surface of the test bar (Fig. 32). The process involved can be analyzed as follows.

In the descending part of the wave, before point A has been reached, the deformation taking place is concentrated to a narrow band. During the course of this deformation, heat is dissipated to the surrounding area, where it causes a decrease in yield stress. Since the surrounding area has undergone only slight work hardening during pre-deformation, i.e., on the ascending part of the first wave, while the narrow band is strongly deformed, a situation is soon reached in which the surroundings of the narrow band are easier to deform than the band itself. For this reason, the deformation spreads into the region surrounding the original band. A deformation front proceeds from the band and in the course of its advance $tg\gamma_1$ increases to the same value it had in the original band. It is possible that some kind of dynamic equilibrium is involved, which just results in constant $tg\gamma_1$. Behind the front, accelerated

ageing phenomena can be thought to take place at high temperature, which lead to an increase in yield stress consistent with the change from A to B (Fig. 29). Another possibility is that the region left behind by the front and where no further deformation occurs, cools down and the yield stress increases for this reason.

When the speed of rotation is very high, as in the test at $n = 160$ r.p.m. with specimens tempered at $T_t = 190^\circ\text{C}$, declining stretches of the $\tau/\text{tg}\gamma$ curves are observed, but there are little or no ascending parts A – B. This can be attributed to the fact that the original deformation band is heated to such degree, and deformation proceeds in it at such a high rate, that it remains the weakest point of the test bar.

4.3.4 Other effects of speed of rotation

In the foregoing, Fig. 30 has been discussed and attempts were made to account for the drop occurring in the φ_{fr}/n curve when the tempering temperature was $T_t = 310^\circ\text{C}$. The same curve has another peculiarity, viz., its rise with increasing n prior to the transition. In order that this phenomenon be understood, it should be kept in mind that the test bar is heated due to the applied torsion, even at a low speed of rotation, and that the rate of work hardening increases with increasing temperature (Figs. 34, 35 and 36). However, it has been noted above that the deformed region spreads out when the rate of work hardening increases. Even the peak of the $\text{tg}\gamma_1/l$ curve, too, already displays increased width at a speed of $n = 0.544$ r.p.m. (Fig. 31). An effect acting in the same direction is also caused by the heat transfer in the undeformed region, where the resistance against deformation lessens. The deformation will then tend to spread into the area which has not undergone work hardening. The speed is not high enough, however, for the attendant temperature rise to be able to cause any concentration of the deformation band.

It is observable from Fig. 30 that at a tempering temperature of $T_t = 70^\circ\text{C}$ the fracturing total twist (φ_{fr}) remains small particularly when the speed (n) is low. The φ_{fr}/n curve jumps upward in the speed interval 0.1 – 1.0 r.p.m. After the jump, it declines at a slow rate with increasing speed. However, the φ_{fr}/n curve for $T_t = 70^\circ\text{C}$ lies above the curves representing any other tempering temperature at the speed of $n = 640$ r.p.m.

The observation can be made from Fig. 34 that the rate of work hardening of the test bars tempered at $T_t = 60^\circ\text{C}$ is particularly high. The same is obviously true for $T_t = 70^\circ\text{C}$. High rate of work hardening results in high yield stresses already at small deformations, as well as in fracture. It should further be kept in mind (cf. page 48) that the test bars tempered at $60\text{--}70^\circ\text{C}$

fail by tensile stress rupture at small speeds, the rupture occurring at low stresses and after small deformation. The reason why this should be so is admittedly unknown. In the range above transition, the bars fail by shearing.

The corresponding φ_{fr}/n curve for $T_t = 430^\circ\text{C}$ is different from any other curves in the respect that it has no jump, but instead a fairly gentle »knee«. The values of φ_{fr} remain small throughout, possibly owing to the fact that the precipitates offer starting points for fractures. At high speeds, the deformation is concentrated to a narrow band at an early stage, obviously for the same reason as in the case of $T_t = 310^\circ\text{C}$ (Fig. 31).

Comparison of the $\tau/tg\gamma$ curves obtained at high and medium speeds (Figs. 28 and 29) reveals that they ascend at a steep rate when the speed of rotation is high. This is most clearly evident in the corresponding curves for $T_t = 430^\circ\text{C}$. At this point the present steel behaves according to the general rule that the resistance of the band to deformation increases with the rate of deformation [46].

4.4 Effect of tempering temperature on the toughness of hardened steel

When the test bars tempered at various temperatures were investigated by tests with the torsion machine, the curves presented in Fig. 38 were obtained at low speed, $n = 0.074$ r.p.m., for the fracturing total twist (φ_{fr}), the energy consumed at fracture (W) and the maximum shear stress (τ_{max}). As can be seen from the φ_{fr}/n curves in Fig. 30, the speed of rotation was such that the test took place below the transition speeds. This means that the deformation spreads far over the neck portion of the test bar and is not concentrated at an early stage. Furthermore, the observation has to be made that the τ/φ and $\tau/tg\gamma$ curves do not become unstable, that is, they do not turn into decline. The fracture thus does not occur until very high values of φ_{fr} and W are met when the tempering temperature is $T_t = 120$ to 390°C .

Low tempering temperatures in the order of 20°C lead to failure by reason of tensile stress when the work hardening is particularly high and the yield stress therefore rises to high values even at small values of φ and $tg\gamma$. As a consequence, the fracturing energy (W) also remains small.

At a high speed ($n = 640$ r.p.m.), the φ_{fr}/T_t and W/T_t curves take an entirely different course from that found at a low speed, as is seen from Fig. 39. In approximately the same range of tempering temperatures, $T_t = 150$ to 350°C , in which a pronounced maximum was encountered at low speed, a definite minimum is now seen. It is to be noted, moreover, that the values of τ_{max} and especially those of φ_{fr} and W are much smaller when the speed is high.

In order to understand this, one should note that the test proceeds in the range above the critical transition speed of rotation in tests where the speed is $n = 640$ r.p.m., while tests at $n = 0.074$ r.p.m. take place below the critical transition speed.

The tempering temperatures $T_t = 390$ to 450 °C lead to small values of the fracturing total twist (φ_{fr}) for the reason that the deformation takes place in a turbulent manner, like that in structures containing incoherent precipitates. Due to the high rate of work hardening, the $\tau/tg\gamma$ curve rises steeply; fracture occurs at small values of $tg\gamma$ and τ_{max} .

It is to be noted in particular that the values of both φ_{fr} and W become comparatively high when the tempering temperature is in the order of 70 °C. As has been observed before, a jump toward higher values then occurs (Fig. 30). This is thought to be due to the fact that at the high speed in question the test bar is heated to such degree that the steel gains in toughness.

In the notched-bar impact test, in which regional spread of the deformation in the test bar has been inhibited by means of the notch, the significance of the unstable character of the deformation remains negligible. It is also conceivable that, owing to the cooling effect produced by the undeformed part of the bar, the unstable condition does not develop and the situation will be the same as in slow torsion tests. This is suggested by the notched-bar impact toughness curve (Fig. 40) on comparison with the fracturing energy (W) curve obtained in a slow torsion test (Fig. 38).

SUMMARY

- I. The effect of tempering upon the toughness of hardened steel has been investigated.

A steel having the nominal analysis: 0.35 % C, 1.5 % Si, 20 % Ni was chosen for this work. The analysis was mainly chosen with the objectives in mind that the M_s temperature should be low enough to ensure that no tempering will occur on quenching, and that the carbides produced on tempering might precipitate each within its own particular tempering temperature range.

Test bars made of the investigated steel were austenitized and quenched in liquid nitrogen, with subsequent isothermal tempering at various temperatures in the range $T_t = -110$ to 450°C .

The structures of the heat-treated specimens were examined by x-rays and by electron microscopy, using both the replica and thin foil technique. Changes occurring in the structures during the tempering process were followed with the aid of a dilatometer.

The principal part of the work consists of mechanical tests, for which a torsion testing machine was designed and built. The machine was so designed that the true stress vs. true strain diagram could be readily obtained with its aid. The experimental conditions, including speed of rotation (n) and testing temperature (T_k), were variable within wide limits. In the mechanical tests performed, the speed of rotation was varied within the range of $n = 0.00135$ to 640 r.p.m. The testing temperatures were: $T_k = -110$, $+25$ and $+95^\circ\text{C}$.

The deformed structures were also examined by electron microscopy.

- II. The x-ray and electron microscopy studies revealed that:

- In the tempering process, ϵ carbide appears in the structure when $T_t = 120$ to 200°C , and cementite when $T_t \geq 400^\circ\text{C}$.
- The results seem to indicate the appearance of an as yet unknown carbide when $T_t = 250$ to 375°C . This carbide was found to deform plastically on torsion.

III. The torsion test results demonstrated that:

- With increasing speed of rotation (n), a discontinuous decrease of the fracturing total twist (φ_{fr}) occurs with the tempering temperatures $T_t = 190$ and 310 °C, and a discontinuous increase with $T_t = 70$ °C, when certain critical speeds of rotation are exceeded. The total twist of specimens tempered at $T_t = 430$ °C decreases uniformly with increasing $\log n$.
- At speeds higher than the critical speed of rotation, work softening occurs in the test bar.
- When work softening occurs, the deformation becomes concentrated in the vicinity of the ultimate fracture in early stages; this is ascribed to a local temperature rise. In addition to the fracturing total twist (φ_{fr}), the fracturing energy (W) then also remains small.
- In torsion tests at low speed, virgin martensite obtained by quenching to -197 °C was found to endure considerable plastic deformation at -110 °C before fracture occurred. Martensite aged at room temperature was, however, completely brittle at -110 °C.
- The concentration of deformation is prevented and the deformation spreads over an extensive region in the torsion test bar when the rate of work hardening is high.
- The rate of work hardening was found to depend on the tempering temperature, which determines the structure of the present steel, in the following manner: $T_t = -110$ °C, moderate; $T_t = 25$ to 60 °C, very high; $T_t = 190$ °C, moderate; $T_t = 310$ °C, very low; and $T_t = 430$ °C, high.
- It may be possible that the variation in the rate of work hardening is caused by differences in respect of the coherent and incoherent precipitates which possibly lead to different modes of deformation.
- At low speeds of rotation, the fracturing total twist (φ_{fr}) and the fracturing energy (W) both obtain high values, and the steel thus presents itself as a tough material when it has been tempered at $T_t = 120$ to 390 °C. At high speeds, again, the fracturing total twist (φ_{fr}) and fracturing energy (W) both obtain their lowest values with almost the same tempering temperatures, $T_t = 150$ to 350 °C. Otherwise, the values of both φ_{fr} and W are some ten times smaller at high than at low speeds.

REFERENCES

1. G. A. Roberts, J. G. Hamaker & A. R. Johnson, Tool steel. Cleveland, ASM, 1962. P. 353.
2. F. R. Palmer & G. V. Luerssen, Tool steel simplified. Reading Penn, Carpenter Steel, 1948. P. 373.
3. J. M. Capus, J. Iron Steel Inst. 201 (1963) p. 54.
4. K. Mazanec & R. Šejnoha, Trans. AIME 233 (1965) p. 1634.
5. G. V. Luerssen, & O. V. Greene, Trans. ASM 32 (1934) p. 321.
6. J. Pietikäinen, Helsinki 1965, [Acta Polytechnica Scandinavica, Ch-Series No. 45].
7. B. C. Woodfine, J. Iron Steel Inst. 173 (1953) p. 247.
8. M. A. Grossman, Iron Age 114 (1924) July 3 p. 149.
9. G. V. Luerssen & O. V. Greene, Trans. ASM 33 (1935) p. 891.
10. B. S. Lement, B. L. Averbach & M. Cohen, Trans. ASM 46 (1954) p. 851.
11. T. A. Read, H. Markus & J. M. McCaughey, Proceedings of the Seminar on the fracturing of metals. Ed. by F. Johansen, W. P. Roop, R. T. Bayless. Cleveland, ASM, 1948. P. 228.
12. N. H. Polakowski, J. Iron Steel Inst. 185 (1957) p. 67.
13. H. Schrader, H. J. Wiester & H. Siepmann, Archiv. f. d. Eisenhüttenwesen 21 (1950) p. 21.
14. P. Payson, Iron Age 168 (1951) Sept. 2 p. 86.
15. J. M. Capus & G. Mayer, Metallurgia 62 (1960) p. 133.
16. M. V. Belous & V. I. Cherepin, Fiz. metal. metalloved. 15 (1963) p. 215.
17. P. G. Winchell & M. Cohen, Trans. ASM 55 (1962) p. 347.
18. C. J. Altstetter, M. Cohen & B. L. Averbach, Trans. ASM 55 (1962) p. 287.
19. G. V. Kurdjumow, J. Iron Steel Inst. 195 (1960) p. 26.
20. G. V. Kurdjumow, Trans. AIME 224 (1962) p. 403.
21. P. M. Kelly & J. Nutting, J. Iron Steel Inst. 197 (1961) p. 199.
22. M. G. Wells, Acta Metallurgica 12 (1964) p. 389.
23. J. P. Snow, Proc. ASTM IV (1904) p. 251.
24. G. Dieter, Mechanical metallurgy. New York, McGraw-Hill, 1961. P. 371.
25. G. V. Luerssen & O. V. Greene, Proc. ASTM 33 Part II (1933) p. 315.
26. G. Dieter, Mechanical metallurgy. New York, McGraw-Hill, 1961. P. 276.

27. N. H. Polakowski & S. Mosfakoy, Trans. ASM 54 (1961) p. 567.
28. F. A. Hodierne, J. Inst. Metals 91 (1963) p. 267.
29. R. H. Richman, Trans. AIME 227 (1963) p. 159.
30. A. M. Hall, Nickel in iron and steel. London, Wiley, 1954. P. 62.
31. H. Modin, Jernkont. Ann. 139 (1955) p. 516.
32. G. Thomas, Transmission electron microscopy of metals. New York, Wiley, 1964. p. 134.
33. R. G. Glenn & J. C. Raley, Philadelphia, 1963. [ASTM Special Technical Publication No. 339]. P. 60.
34. G. Dieter, Mechanical metallurgy. New York, McGraw-Hill, 1961. P. 280.
35. W. Truszkowski & Z. Jasienski, J. Inst. Metals 92 (1964) p. 225.
36. G. Dieter, Mechanical metallurgy. New York, McGraw-Hill, 1961. P. 273.
37. G. Dieter, Ibid. p. 479.
38. K. H. Jack, J. Iron Steel Inst. 169 (1951) p. 26.
39. Ya. I. Kagan, S. V. Bronin & I. Ya. Sidorenko, Metallovedenie i termicheskaya obr. met. No. 2 (1964) p. 29.
40. A. W. Sleeswyk, Acta Metallurgica 8 (1960) p. 130.
41. G. Dieter, Mechanical metallurgy. New York, McGraw-Hill, 1961. P. 287.
42. A. Kelly & R. B. Nicholson, Progress in Material Science, Vol. 10. London, Pergamon, 1963. P. 313.
43. A. Kelly & R. B. Nicholson, Ibid. p. 315.
44. A. Kelly & R. B. Nicholson. Ibid. p. 310.
45. R. E. Smallman, Modern physical metallurgy. London, Butterworths, 1962. P. 223.
46. D. McLean, Mechanical properties of metals. New York, Wiley, 1962. P. 133.
47. R. E. Smallman, Modern physical metallurgy. London, Butterworths, 1962. P. 209.

Teknillisen korkeakoulun kirjasto